

A COMPUTATIONAL ANALYSIS ON ROTOR-PROPELLER ARM  
INTERACTION IN HOVERING FLIGHT

A THESIS SUBMITTED TO  
THE GRADUATE SCHOOL OF NATURAL AND APPLIED SCIENCES  
OF  
MIDDLE EAST TECHNICAL UNIVERSITY

BY

SERKAN YENER

IN PARTIAL FULFILLMENT OF THE REQUIREMENTS  
FOR  
THE DEGREE OF MASTER OF SCIENCE  
IN  
AEROSPACE ENGINEERING

SEPTEMBER 2019



Approval of the thesis:

**A COMPUTATIONAL ANALYSIS ON ROTOR-PROPELLER ARM  
INTERACTION IN HOVERING FLIGHT**

submitted by **SERKAN YENER** in partial fulfillment of the requirements for the degree of **Master of Science in Aerospace Engineering Department, Middle East Technical University** by,

Prof. Dr. Halil Kalıpçılar  
Dean, Graduate School of **Natural and Applied Sciences**

\_\_\_\_\_

Prof. Dr. İsmail Hakkı Tuncer  
Head of Department, **Aerospace Engineering**

\_\_\_\_\_

Assist. Prof. Dr. Mustafa Perçin  
Supervisor, **Aerospace Engineering, METU**

\_\_\_\_\_

**Examining Committee Members:**

Assoc. Prof. Dr. Utku Kânoğlu  
Aerospace Engineering, METU

\_\_\_\_\_

Assist. Prof. Dr. Mustafa Perçin  
Aerospace Engineering, METU

\_\_\_\_\_

Assoc. Prof. Dr. Nilay Sezer Uzol  
Aerospace Engineering, METU

\_\_\_\_\_

Assist. Prof. Dr. Ali Türker Kutay  
Aerospace Engineering, METU

\_\_\_\_\_

Assist. Prof. Dr. Munir Elfarra  
Aerospace Engineering, Ankara Yıldırım Beyazıt University

\_\_\_\_\_

Date: 11.09.2019

**I hereby declare that all information in this document has been obtained and presented in accordance with academic rules and ethical conduct. I also declare that, as required by these rules and conduct, I have fully cited and referenced all material and results that are not original to this work.**

Name, Surname: Serkan Yener

Signature:

## **ABSTRACT**

### **A COMPUTATIONAL ANALYSIS ON ROTOR-PROPELLER ARM INTERACTION IN HOVERING FLIGHT**

Yener, Serkan  
Master of Science, Aerospace Engineering  
Supervisor: Assist. Prof. Dr. Mustafa Perçin

September 2019, 84 pages

This study presents a computational analysis on the interaction between rotor and different rotor frame-arm geometries in hovering flight. The influence of the frame arm on the aerodynamic performance of the rotor is assessed by using commercially available computational fluid dynamics (CFD) solver ANSYS Inc. Fluent 17. Numerical results are validated for hovering and vertical climb flight conditions with thrust and torque measurements conducted on a 16x4 carbon fiber propeller. The thrust and torque measurements were performed in the test section of the low-speed METUWIND C3 wind tunnel at the Rüzgem (Metuwind). After validating the numerical simulations with the thrust and torque measurement results of the 16x4 carbon fiber propeller, four different arm geometries (i.e., Eppler Arm, 25mm cylindrical tube, 25mm square tube, and 25mm square tube with a 10mm slot) are created, and added to the validated CFD model to assess their effect on the aerodynamic performance of the rotors. The results of this study reveal that the propeller-Eppler arm configuration has 4.89%, 21.59%, and 5.18% greater propeller efficiency than that of the propeller-cylindrical arm, propeller-square arm, and propeller-slotted square arm configurations, respectively.

Keywords: Propeller performance, Rotor performance experiment, Quadro rotor arm, Rotor arm interaction, CFD

## ÖZ

### **PERVANE VE PERVANE KOLU ARASINDAKİ ETKİLEŞİMİN HAVADA TUTUNAN UÇUŞ DURUMU İÇİN HESAPLAMALI YÖNTEMLE ANALİZ EDİLMESİ**

Yener, Serkan  
Yüksek Lisans, Havacılık ve Uzay Mühendisliği  
Tez Danışmanı: Dr. Öğr. Üyesi Mustafa Perçin

Eylül 2019, 84 sayfa

Bu çalışmada, askıda uçuş durumu için pervane ve farklı pervane kolu geometrileri arasındaki etkileşimin hesaplamalı yöntemle yapılmış bir analizi sunulmaktadır. Pervane kolunun pervanenin aerodinamik performansı üzerindeki etkisi, ticari olarak temin edilebilen Hesaplamalı Akışkanlar Dinamiği (HAD) çözücü yazılımı ANSYS Inc. Fluent 17 kullanılarak değerlendirilmiştir. Sayısal sonuçlar, bir 16x4 karbon fiber pervane kullanılarak yapılan itme ve tork ölçümleri ile askıda uçuş ve dikey uçuş koşulları için doğrulanmıştır. İtme ve tork ölçümleri, ODTÜ Rüzgem'deki düşük hızlı METUWIND C3 rüzgar tünelinin test bölümünde gerçekleştirilmiştir. 16x4 karbon fiber pervanenin sayısal simülasyonu itme ve tork ölçüm sonuçları ile doğruladıktan sonra, dört farklı pervane kol geometrisi (Eppler tipi, 25mm çaplı silindirik boru, 25mm kenarlı kare boru, ve ortasında 10mm olukdan oluşan 25mm kenarlı kare boru) oluşturulup pervanenin aerodinamik performansı üzerindeki etkilerini değerlendirmek için HAD modeline eklenmiştir. Pervane kolu geometrileri arasındaki pervane verimi karşılaştırmasının sonuçları, Eppler kol geometrisinin benzer ebatlı silindir pervane koluna göre % 4.89, benzer ebatlı kare kesitli pervane koluna kıyasla % 21.59 ve aynı kare kesitli pervane kolunun oluklu versiyonundan % 5.18 daha verimli olduğunu göstermektedir.

Anahtar Kelimeler: Pervane performansı, Rotor performans deneyi, Quadrotor kolu,  
Rotor kolu etkileşimi, HAD

This work is dedicated to Themis and Armazi

## ACKNOWLEDGEMENTS

I would like to thank the people who have helped at the various stages of my thesis research. First and foremost, the guidance and advice provided by my advisor, Assist. Prof. Dr. Mustafa Perçin was invaluable throughout this rewarding project.

I would like to extend my deepest gratitude to Assoc. Prof. Dr. Nilay Sezer Uzol for her support and giving me the opportunity of studying in METU Aerospace Engineering Department.

I would also like to acknowledge Assist. Prof. Dr. Ali Türker Kutay for all his support regarding the experimental equipment which I used in this study.

Special thanks to Dr. Human Amiri, Murat Erbaş, Hasan Çakır, Halit Kutkan, Ali İhsan Gölcük, Mahdi Yazdanpanah, Derya Kaya and my car Renault Clio for their contributions to this study and friendships.

I would like to express my eternal gratitude to my parents, Mine and İshak, for their love and support throughout my life.

At last but not least, I want to express my love and appreciation to my fiancée, Merve Önerli, who has propelled me to complete my thesis.

## TABLE OF CONTENTS

ABSTRACT .....	v
ÖZ .....	vii
ACKNOWLEDGEMENTS .....	x
TABLE OF CONTENTS .....	xi
LIST OF TABLES .....	xiv
LIST OF FIGURES .....	xv
LIST OF ABBREVIATIONS .....	xix
LIST OF SYMBOLS .....	xx
CHAPTERS	
1. INTRODUCTION .....	1
1.1. Literature Survey .....	3
1.1.1. Experimental method .....	6
1.1.2. Numerical method .....	9
1.1.2.1. Low-fidelity numerical technique .....	9
1.1.2.2. High-fidelity numerical technique .....	10
1.2. Previous Studies on Rotor Frame-arm .....	17
1.3. Aim and Structure of the Thesis .....	18
2. EXPERIMENTAL SETUP AND METHODOLOGY .....	21
2.1. Wind Tunnel Facility .....	21
2.2. Experimental Setup .....	22
2.3. Testing Procedure .....	25
2.4. Data Reduction and Validation .....	27

2.4.1. Uncertainty analysis .....	28
2.4.2. Repeatability of the test measurements .....	29
2.4.3. Comparison of propeller measurements .....	31
3. NUMERICAL ANALYSIS AND METHODOLOGY .....	37
3.1. Computational Fluid Mechanics Differential Equations .....	37
3.1.1. Continuity equation .....	37
3.1.2. Momentum conservation equations.....	37
3.1.3. Turbulence modeling.....	38
3.2. CFD Modelling Methodology.....	41
3.2.1. Simulation approach.....	41
3.2.2. Flow domain and boundary conditions .....	43
3.2.2.1. SIMPLE algorithm.....	46
3.2.3. Mesh generation .....	47
3.3. Rotor Frame-arm Interaction Study .....	50
3.3.1. MRF model approach.....	51
3.4. Numerical Method Verification and Validation .....	53
3.4.1. Mesh and iteration number independency analysis.....	53
3.4.2. Model independency analysis .....	57
4. RESULTS AND DISCUSSION .....	61
4.1. Carbon Fiber 16x4 Propeller Test and CFD Results.....	61
4.1.1. Hovering flight results.....	61
4.1.2. Vertical climb flight results .....	63
4.2. Rotor Frame-arm Interaction Study Results .....	64
4.2.1. Examining the consistency of MRF approach in itself .....	65

4.2.2. Performance comparison with and without the presence of the arm .....	67
4.2.3. Effect of the different rotor frame arm shapes.....	68
4.2.4. Rotor frame arm distance effects .....	73
5. CONCLUSION.....	77
REFERENCES.....	81

## LIST OF TABLES

### TABLES

Table 2.1. Thrust and Torque measurement conditions .....	27
Table 2.2. Thrust and Torque uncertainty estimates.....	29
Table 2.3. Thrust and Power coefficient comparison data for hovering flight.....	33
Table 2.4. Thrust and Power coefficient comparison data for vertical climb flight..	35
Table 3.1. CFD simulation conditions .....	43
Table 3.2. Boundary conditions for the flow domain in hovering flight simulations	45
Table 3.3. Boundary conditions for the flow domain in vertical climb flight simulations.....	45
Table 3.4. Solution Methods.....	46
Table 3.5. Mesh Sizing Parameters .....	49
Table 3.6. Number of Mesh Cells.....	53
Table 4.1. Thrust and Power coefficient comparison data for hovering flight .....	62
Table 4.2. Thrust and Power coefficient comparison data for vertical climb flight .	64
Table 4.3. Average Efficiency, Thrust and Power coefficient values of different rotor arm shapes .....	71
Table 4.4. Average Efficiency, Thrust and Power coefficient values of Eppler and Slotted square arm at the different rotor arm distances .....	75

## LIST OF FIGURES

### FIGURES

Figure 1.1. <b>(a)</b> Fixed-wing UAV [3], <b>(b)</b> Flapping-wing UAV [4] , <b>(c)</b> Rotary-wing UAV [5] .....	1
Figure 1.2. Breguet-Richet Gyroplane [6] .....	2
Figure 1.3. Propeller Diameter [10] .....	4
Figure 1.4. Reynolds number spectrum [11].....	5
Figure 1.5. <b>(a)</b> Experimental testing rig designed by Brandt [15], <b>(b)</b> UIUC wind tunnel.....	7
Figure 1.6. <b>(a)</b> Quadrotor simulation domain, <b>(b)</b> Boundary conditions, and distances of the control volume [36].....	17
Figure 1.7. <b>(a)</b> 25mm tube, <b>(b)</b> nacelle, <b>(c)</b> 10mm square tube [38], <b>(d)</b> Slim-arm model, <b>(e)</b> U-arm model [37] .....	18
Figure 2.1. METUWIND C3 wind tunnel .....	21
Figure 2.2. Experimental setup with <b>(a)</b> APC Slow Flyer 11x4.7 and <b>(b)</b> Carbon fiber 16x4 propeller .....	22
Figure 2.3. <b>(a)</b> Dwyer Model 471B thermo-anemometer [41], <b>(b)</b> Extech SD700 barometric pressure/humidity/temperature data logger [42].....	23
Figure 2.4. <b>(a)</b> ATI Gamma loadcell [22], <b>(b)</b> Quanum brushless motor, <b>(c)</b> RPM sensor with the test setup.....	24
Figure 2.5. <b>(a)</b> Data acquisition setup, <b>(b)</b> NI Compact DAQ-9178 data acquisition chassis [43], <b>(c)</b> DC power supply .....	24
Figure 2.6. Thrust repeatability data for APC Slow Flyer 11x4.7 propeller for hovering flight .....	30
Figure 2.7. Torque repeatability data for APC Slow Flyer 11x4.7 propeller for hovering flight.....	30

Figure 2.8. Thrust coefficient repeatability data for APC Slow Flyer 11x4.7 propeller for vertical climb flight.....	31
Figure 2.9. Power coefficient repeatability data for APC Slow Flyer 11x4.7 propeller for vertical climb flight.....	31
Figure 2.10. Thrust coefficient comparison data for APC Slow Flyer 11x4.7 propeller for hovering flight.....	32
Figure 2.11. Power coefficient comparison data for APC Slow Flyer 11x4.7 propeller for hovering flight.....	33
Figure 2.12. Thrust coefficient comparison data for APC Slow Flyer 11x4.7 propeller for vertical climb flight.....	34
Figure 2.13. Power coefficient comparison data for APC Slow Flyer 11x4.7 propeller for vertical climb flight.....	34
Figure 3.1. Three main phases of CFD [36] .....	42
Figure 3.2. Simulation procedure .....	42
Figure 3.3. 16-inch carbon fiber propeller and 3D scanned 16-inch carbon fiber propeller.....	43
Figure 3.4. <b>(a)</b> Flow domain and boundary conditions, <b>(b)</b> Rotating domain.....	44
Figure 3.5. Overview of the SIMPLE solution algorithm working principle.....	47
Figure 3.6. A portion of the mesh with respect to the propeller blade surface, propeller blade tip, and 0.75% blade span position .....	48
Figure 3.7. Isometric view of flow domain including arm structure with 16-inch propeller.....	50
Figure 3.8. E 862 strut airfoil [46].....	51
Figure 3.9. <b>(a)</b> Eppler Arm, <b>(b)</b> Cylinder Arm, <b>(c)</b> Square Arm, <b>(d)</b> Slotted Square Arm.....	51
Figure 3.10. Six different phases used for the arm interaction study .....	52
Figure 3.11. Examples of coarse, medium, and fine mesh generated on the propeller surface <b>(a)</b> coarse surface mesh, <b>(b)</b> medium surface mesh, <b>(c)</b> fine surface mesh ..	54
Figure 3.12. Mesh independency study results for hovering flight at 2000 rpm.....	55
Figure 3.13. Mesh independency study results for vertical climb flight at 2000 rpm	55

Figure 3.14. $y +$ contour of the propeller with cylinder arm.....	56
Figure 3.15. Residuals for 2000 rpm vertical climb flight simulation.....	57
Figure 3.16. Thrust value comparison between the measurement data and different turbulence models at 2000rpm for hovering flight .....	58
Figure 3.17. Torque value comparison between measurement data and different turbulence models at 2000rpm for hovering flight .....	58
Figure 3.18. Thrust value comparison between measurement data and different turbulence models at 2000rpm for vertical climb flight.....	59
Figure 3.19. Torque value comparison between measurement data and different turbulence models at 2000rpm for vertical climb flight.....	59
Figure 4.1. Comparison of the thrust values obtained from CFD simulations and measurements for the Carbon Fiber 16x4 propeller in hovering flight .....	61
Figure 4.2. Comparison of the torque values obtained from CFD simulations and measurements for the Carbon Fiber 16x4 propeller in hovering flight .....	62
Figure 4.3. Comparison of the thrust coefficient obtained from CFD simulations and measurements for the Carbon Fiber 16x4 propeller in vertical climb flight .....	63
Figure 4.4. Comparison of the power coefficient obtained from CFD simulations and measurements for the Carbon Fiber 16x4 propeller in vertical climb flight .....	63
Figure 4.5. Comparison of the thrust coefficients obtained from CFD simulations for the different arm shapes with respect to the different propeller phase angles .....	66
Figure 4.6. Comparison of the thrust coefficient averages for the different arm shapes with respect to the different propeller phase numbers .....	66
Figure 4.7. Pressure contours with and without the presence of the small distance square arm with respect to the center of the arm at the 0° rotor phase .....	67
Figure 4.8. Pressure contours with and without the presence of the small distance square arm with respect to the center of the arm at the 90° rotor phase .....	67
Figure 4.9. Pressure contours of the four different arms with respect to the center of the arm at the 0° rotor phase .....	68
Figure 4.10. Velocity contours at the 90° rotor phase for different arm shapes .....	70
Figure 4.11. 3D vorticity magnitude representation of flow for the different arms...	72

Figure 4.12. A sketch of small rotor frame-arm distance configuration in mm ..... 73  
Figure 4.13. The pressure contour of the slotted square and Eppler arm with respect to  
the center of the arm for the small rotor frame-arm distance ..... 74

## LIST OF ABBREVIATIONS

BART	Basic Aerodynamics Research Tunnel
BEMT	Blade Element Momentum Theory
BET	Blade Element Theory
BSL-RSM	Baseline-Reynolds Stress Model
CFD	Computational Fluid Dynamics
CMBET	Combined Momentum Blade Element Theory
HALE	High Altitude Long Endurance
METU	Middle East Technical University
MRF	Multi Reference Frame
RANS	Reynolds Average Navier Stokes
RC	Remote Controlled
SIMPLE	Semi Implicit Method for Pressure Linked Equations
SST	Shear Stress Transport
UAS	Unmanned Air Systems
UAV	Unmanned Air Vehicle
UIUC	University of Illinois at Urbana-Champaign
VTOL	Vertical Take-Off/Landing

## LIST OF SYMBOLS

A	Disk area of propeller
$C_P$	Propeller power coefficient
$C_T$	Propeller thrust coefficient
D	Diameter of propeller
J	Propeller advance ratio
k	Coverage factor or turbulent kinetic energy
N	Rotational speed of the propeller (rpm) or number of samples
P	Pressure or Power of propeller
Q	Torque of propeller
R	Propeller radius or ideal gas constant for air
Re	Reynolds number
T	Thrust
$t_{air}$	Air temperature
U	Expanded uncertainty
V	Absolute velocity or velocity of propeller
$\rho$	Air density
$\hat{V}$	Estimated value
$\delta$	Kronecker delta function
$\bar{M}$	Measured mean value

$\sigma$	Measured standard deviation
$\mu$	Molecular viscosity
$\sigma_k$ and $\sigma_\omega$	Prandtl numbers for $k$ and $\omega$
$\eta$	Propeller propulsion efficiency
$\vec{r}$	Radius of cell center from the rotation axis
$\Omega_{ij}$	Rotation rate
$\omega$	Specific dissipation
$\bar{\tau}$	Stress tensor
$\mu_t$	Turbulent viscosity



## CHAPTER 1

### INTRODUCTION

There are millions of species of birds, insects, and sea creatures in the world. These creatures' peculiar characteristics enable them to move successfully at very low Reynolds numbers. Successful movements of these creatures have attracted the attention of researchers, and many studies have been conducted on this subject. Observations and studies in this area formed the basis of Unmanned Aerial Vehicles/Systems (UAV / UAS).

UAV usage areas are increasing day by day with the increase in battery life and cheaper electronic flight elements (such as sensors, microprocessors). UAVs have been the focal point of aviation since the first flight in 1903. Today, they find use in many different areas such as target detection and monitoring, surveillance, search and rescue in hazardous areas, pesticides, traffic monitoring, and mapping [1], [2]. The remote control of these vehicles and the absence of pilots in them, eliminate the risk of endangering human life in many ways.

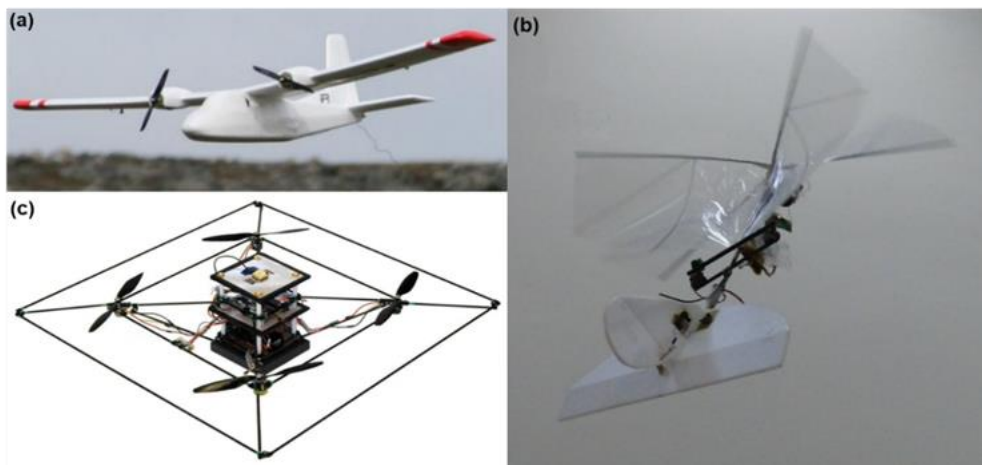


Figure 1.1. (a) Fixed-wing UAV [3], (b) Flapping-wing UAV [4] , (c) Rotary-wing UAV [5]

UAVs can be classified in terms of their features such as weight, engine types, flight range, maximum altitude, speed, and wingspan size. Extensively, UAV designs that are being studied today are fixed-wing (Figure 1.1a), flapping-wing (Figure 1.1b), and rotary-wing (Figure 1.1c).

The use of UAVs which can be accessing the challenging terrains with the capability of maneuvering and having vertical take-off/landing (VTOL), is increasing day by day. An aircraft capable of making VTOL has many different configurations, and it can be a helicopter with two rotors, a three-rotor tricopter, a four-rotor quadrocopter, six-rotor hexacopter.

A quadrotor is an aerial vehicle which has four rotors mounted in cross configuration [7]. The initial studies on quadrotors date back to the beginning of the 1900s. In 1907, the four-rotor helicopter produced by Louis Breguet in France was the first known quadrotor, shown in Figure 1.2.

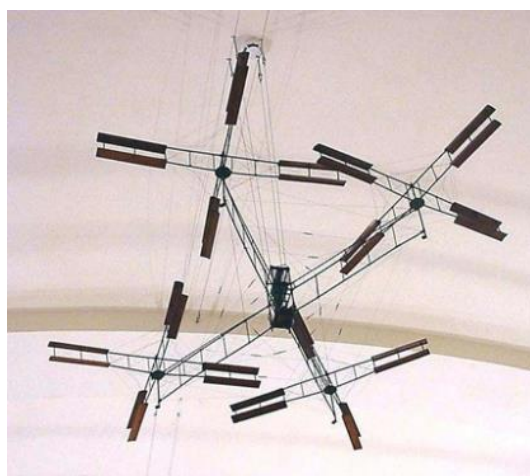


Figure 1.2. Breguet-Richet Gyroplane [6]

Having high maneuverability and VTOL capability enable quadrotors to handle many challenging tasks. VTOL and hovering are the most significant differences that separate rotary wing UAVs from other aircraft. Quadrotors draw attention with two essential advantages among all other UAVs that can maintain VTOL. First, instead of complicated mechanical control linkages in a helicopter, fixed-pitch rotors are used

for the actuation of the rotor. So, vehicle control is done by changing the speed of the motor, which facilitates both the design and maintenance of the quadrotor. Second, due to the usage of four propellers in the quadrotor, the ratio of each propeller diameter to the quadrotor body is smaller than the ratio of the helicopter's main rotor diameter to the helicopter fuselage. In this way, each rotor is separately causing less kinetic energy storage of the rotor during the flight. This reduces the risk of fragmentation when the rotor contacts an object [5].

In today's conditions, especially in military applications, there is a growing need for rotary wing UAVs with high maneuverability in surveillance missions to operate in challenging conditions. Since the quadrotors are considerably cheaper than the helicopters and are suitable for surveillance, search and rescue operations, designers tend to use them in more fields efficiently. Nevertheless, the payload capacity of most drones is insufficient to carry heavy components. Therefore, improving the geometrical characteristics has been considered a way of developing the payload capacity. The development of technology enables the widespread use of UAVs. This situation leads to the need for performance improvement of UAV platforms. In order to address this need, in this chapter, the literature survey on the aerodynamic performance of quadrotor propellers and rotor frame arm will be first explained. Then, the aim and structure of the thesis will be presented.

### **1.1. Literature Survey**

UAVs have become a rapidly growing aviation discipline in the field of military and civil aviation. In addition to their function as hobby items in the form of model airplanes, they are designed to transport small loads and are mostly utilized for surveillance and research needs [7].

Recent increase of interest in the field of UAVs has stimulated attention to rotary wing aerodynamics. The development of aviation has also been connected to the developments in propellers as well as the design of the air vehicles. That is why,

propellers for air vehicles are still relevant today, as in the past. For this reason, aerodynamic, structural, and performance studies of propellers are ongoing. After the first flight by Wright brothers, which is considered a turning point in aviation, intensive works have been dedicated to the development of propellers.

A propeller as the primary component of UAV, is a rotating wing consisting of different airfoils connected to each other in a way to make a twisted wing. It is a device having a revolving hub with a minimum of two blades [8].

Propellers, also called an airscrew, transform rotary motion from an engine shaft or another power source to thrust which is generated for aircraft to move forward while pushing the air in the adverse way [9].

Diameter and pitch measurements of propellers are used to identify the propeller. Figure 1.3 shows the diameter of a propeller. The pitch of propeller can be described as the distance which the propeller will move forward in one revolution [10]. In this study, propeller size is given in inches; for example, the 16x4 propeller defines a diameter measurement of the 16-inch with a 4 in/revolution pitch measurement.



Figure 1.3. Propeller Diameter [10]

Most of the UAV's utilize a rotor operating in the Reynolds number range of  $10^3$  to  $10^6$ . It is shown in the Reynolds number spectrum in Figure 1.4, which is defined by Lissaman [11]. There is not enough data on small-scale propellers that operate at low Reynolds numbers while propeller performance for full-scale conventional aircraft has been well documented [12]. As Deters et al. denoted, it is not easy to estimate the performance of low Reynolds number of propellers. As a result, limited investigation has been done for low Reynolds numbers [7]. Accordingly, it is necessary to study the

propeller performance and various other components of UAVs at low Reynolds numbers.

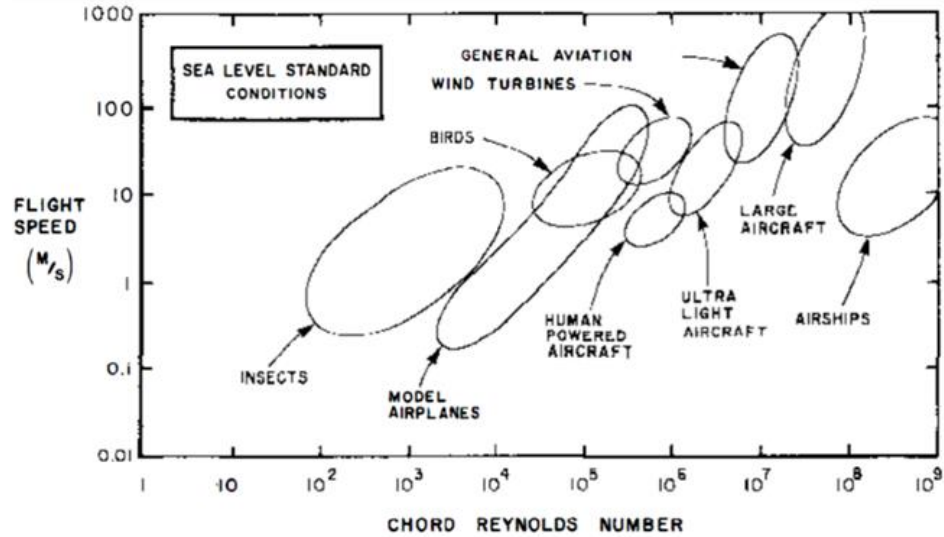


Figure 1.4. Reynolds number spectrum [11]

For designers, propellers exhibit a sophisticated design that includes integrity of aerodynamics, thrust performance, and structure. Therefore it can be said that the development of the propellers was relatively slow comparing to the development in aviation technology such as jet engines, navigation instruments, etc. [13]. Parallel to the development of new technology today, new usages for propellers have been emerged. Propeller design of rotary wings requires more attention than the other types, and because of being a different aerodynamic phenomenon, it is crucial to do research on propellers design, and determine if they lead to reliable performance. There are different methods for calculating the performance of propellers. These can be sorted as experimental and numerical methods. While it is possible to create real conditions with experimental methods, it is disadvantageous in terms of cost and time compared to the numerical methods. Numerical methods enable more complex situations to be simulated with the results that are closer to reality and need more solution time and hardware requirements [14]. From this point onwards, some important propeller performance studies with experimental and numerical methods will be presented.

### **1.1.1. Experimental method**

In the experimental method, the propeller, whose performance values are to be measured, is positioned inside a wind tunnel for both hovering and vertical climb flight conditions. Researchers carried out experiments to understand the propeller performance at low Reynolds numbers. In the following sections, similar experimental studies will be summarized in terms of the wind tunnel, propeller, and flight characteristics.

In their experimental study, Brandt and Selig [12] pointed out the importance of rotor performance at low Reynolds numbers for designing and performance analysis of UAVs. They made wind tunnel thrust and torque measurements of 79 commercial rotors at the diameter range of 7 to 13 inch which are used on small UAVs, and model aircraft. Measurements were obtained in a low-turbulence subsonic wind tunnel (Figure 1.5) having a rectangular cross-section of 2.8x4.0 ft at the University of Illinois at Urbana-Champaign (UIUC). The experiments were carried out at various wind tunnel speeds with propeller rotational speeds ranging from 1500 to 7500 revolutions per minute (RPM). They showed that the operation range of Reynolds number affects the overall aircraft performance, and as the Reynolds number on the propeller increases, the efficiency of the propeller increases. It was stated that the reason for this increase was because of the increase in thrust or a decrease in power. Deters and et al. [7] extended the study of Brandt and Selig by applying the same experimental method with 27 different propellers, four of which were manufactured with a 3D printer. In their study, the influence of low Reynolds numbers on small-scale propellers was explored and, the slipstream characteristics of small-scale propellers were specified. Different scale 3D printed propellers were tested at the same Reynolds number, and approximately identical performance outcomes were obtained.

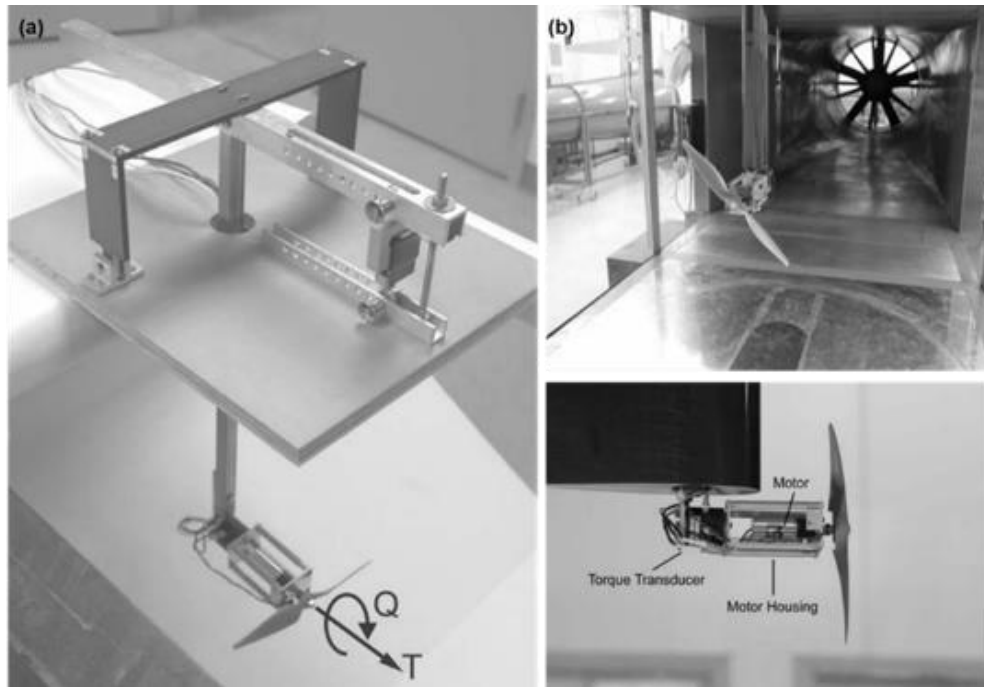


Figure 1.5. (a) Experimental testing rig designed by Brandt [15], (b) UIUC wind tunnel

In another study on propellers, Merchant [16] designed, developed, and validated an Integrated Propulsion Test System, and discussed the prominent features of this measurement system. Wichita State University's 3x4 ft low-speed wind tunnel was used to conduct the performance measurements of over 60 small-scale propellers. Valid and reliable performance data of 6 to 22 inch propellers operating at a Reynolds number between 30,000 and 300,000 were charted. They examined the performance results of the two identical propellers manufactured by the same manufacturers. The wooden propeller of one of the manufacturers exhibited a discrete difference in propeller performance results. Nowadays, researchers commonly take advantage of performance datasets of Merchant and Brandt. Because obtaining valid and reliable datasets is challenging to do and involves much effort and facility.

Similarly, Bağçe [9] determined the performance of Turbotek mini aircraft propellers by using the 2.46x1.64x7.87 ft wind tunnel of the Mechanical Engineering Department at METU with the test equipment specially designed for the study. Thrust,

power, and efficiency measurements of four different Turbotek propellers were taken for vertical climb and hovering flight configurations. The results obtained from the experiment were observed to be satisfactory in comparison to Turbotek's analytical and computational fluid dynamics (CFD) results.

Gamble and Arena [10] also performed wind tunnel tests with the propellers ranging in diameter from 14 to 24 inch with Reynolds numbers of 40,000 to 200,000. They observed an efficiency dependence on the low Reynolds numbers for Advanced Precision Composites (APC) 18x12 and 18x8 propellers. Experimental results showed that the efficiency of the APC 18x12 propeller increased by 5% with the increase in Reynolds number from 40,000 to 100,000. They also clearly showed that low Reynolds numbers had a substantial effect on the pitch of the small propeller.

Similarly to Deters's study [7], Tracy [17] carried out an experimental study to design and analyze a pusher propeller for a small UAV. SolidWorks, QMIL, and QPROP programs were used to manufacture the propeller design. Experimental measurements were conducted in a 1x1 ft wind tunnel to investigate the effect of fuselage blanketing on four different propellers performance. It was empirically found that four of the blanketed propellers had higher power consumption compared to the free airstream without any blankets. Around the same time at Oklahoma State University (OSU)'s wind tunnel, propellers of Bettinger [18] were also being manufactured and tested. At the end of the study, test analysis of the propeller was evaluated to be comparable in both strength and performance.

In their experimental study, Baranski et al. [19] made vertical wind tunnel thrust, torque, and rotational speed measurements of 28 commercial rotors at the diameter range of 17 to 24 inch. The study aimed to identify the optimal propeller for an existing engine in order to enhance mission duration. They developed a method for performance comparison of the propellers. They proposed that for matching engine and propeller, experimental data was compulsory due to the lack of reliable data from small engine manufacturers. It was discovered that even among the propellers of the

same diameter from different manufacturers, the range could be increased up to 100 miles (20% increase) with proper engine and propeller combination.

## **1.1.2. Numerical method**

### **1.1.2.1. Low-fidelity numerical technique**

In the low-fidelity numerical solution method of rotating propellers, Goldstein's Vortex, Momentum, and Blade Element Theories (BET) have been utilized to compute the steady-state flow over the propellers. Blade Element Momentum Theory (BEMT), which provides inconsistent outcomes at high advance ratios and along the inner half span of the propeller, is the combination of Blade Element and Momentum Theories [9]. For evaluating the propeller performance, similar low-fidelity numerical studies will be summarized in the following parts, in terms of their numerical solution and validation method.

In the study of Moffitt et al. [20], where they validated the Vortex Propeller Theory for UAV design with uncertainty analysis, they submitted vortex theory formulations and the wind-tunnel test result comparisons of the propellers. They used the XFOIL Subsonic Airfoil Development System software that is used for the design and analysis of subsonic isolated airfoils for airfoil modeling. As a result of this study, it was seen that the model could estimate the propeller performance in an extensive range of circumstances correctly, while both thrust and power were overestimated at low advance ratios.

Stajuda et al. [21] emphasized the need for experimental research for theoretical development in the field of propeller design. They stated that BET and BEMT could be used to assess the aerodynamic performance of propellers. However, these methods require experimental data for the sake of validation.

Combining both low-fidelity numerical solution and experimental methods, Kaya [22] developed mathematical models to predict the aerodynamic performance of a quadrotor for various flight conditions. BET and BEMT were used for forming a low-

fidelity numerical model, and parameters of these mathematical models were defined with the experimental measurements acquired from METU Rüzgem wind tunnel.

Demirtaş [23] and Pamuk [13] both designed propeller blade using NACA 4412 airfoil in their studies. Local Mach numbers, lift and drag coefficients were acquired by utilizing CFD ANSYS Fluent software at each cross-section of the propeller. By using this data, different airfoil geometries were optimized to manufacture new propellers. As a result of these studies, it was seen that ANSYS Fluent software could be a useful tool for defining the aerodynamic characteristics of the blade profiles.

Similar to the above numerical studies, Zeune et al. [24] comprehensively compared wind tunnel test and numerical prediction of the propellers ranging in diameter from 6 to 20 inch. Larger propellers were tested at a vertical wind tunnel, and the small propellers were tested at Basic Aerodynamics Research Tunnel (BART). Some of the wind tunnel test results were compared with Brandt's results [15]. Blade geometries of Graupner 10x8 and Aeronaut 12x8 propellers were acquired by digital scans, while the geometry of APC 18x14 propeller was dimensioned from the physically sliced propeller blade sections. Numerical and experimental comparisons of the propellers were carried out with the BEMT code, and it was found that in some way, the BEMT results were very delicate to the proper interpretation of propeller twist, chord distributions, and the Reynolds number of the airfoil sections.

#### **1.1.2.2. High-fidelity numerical technique**

The high-fidelity numerical analysis method uses CFD simulation that generally takes the advantage of the Reynolds-average Navier–Stokes (RANS) equation to determine flow properties. With incremental developments in computer technologies, CFD methods have become a substantial and remarkably useful tool for propeller design and analysis. Besides, advancements in high-fidelity numerical methods have led to more design variables to be simulated more accurately and in a more reliable way than before. In order to evaluate propeller performance, CFD simulations were successfully

performed. Some of these numerical studies will be summarized in the following paragraphs, in terms of their flow domain features, propeller types, mesh features, and solution methods. The software used for propeller design and CFD simulations will also be mentioned.

In their comprehensive numerical study, Ramakrishna et al. [25] carried out a ship propeller performance and cavitation simulation study by using CFD analysis software ANSYS Fluent. Propeller model geometry was created with the help of CATIA V5R20 CAD software. The ship propeller was put into the center of the enclosed cylinder flow domain, and the distance between the propeller and the inlet of the domain was  $3D$ , where  $D$  is the propeller blade diameter. The distance between the propeller and the outlet of the domain was  $4D$ . The diameter of the enclosed cylinder was described  $4D$ . For this study, the structural grid with hexahedral cells were generated with ICEM CFD software throughout the entire flow domain and propeller. 1.3 million hexahedral cells were generated for the simulation flow domain.

For propeller performance analysis solution, the  $k-\varepsilon$  turbulence model was utilized. Multi reference frame (MRF) was appointed to cell zone conditions with a rotational velocity of 3000rpm, 2400rpm, 1800rpm, and 1500rpm. Thrust and torque coefficient achieved from CFD results agreed well with the experimental results obtained by Salvatore et al. [26] with maximum 0.013 and minimum 0.001 differences. The results showed that CFD could be used to analyze open water characteristics and cavitation phenomena of a propeller with quite reasonable accuracy.

In the study of Morgut and Nobile [27], where they numerically investigated the influence of grid type and turbulence model for marine propeller, they used the CFD CFX 11 software for comparison of the Shear Stress Transport (SST) turbulence model and the Baseline-Reynolds Stress Model (BSL-RSM) turbulence model for steady state conditions. The influences of hexa-structured and hybrid-unstructured meshes were analyzed only around the propeller region. Experimental data of the four-bladed propeller E779A and the five-bladed propeller P5168 were used to validate the

numerical results. Enclosed cylinder flow domain consisting of two-cylinder flow domain, known as rotating and fixed domain, was created for the numerical predictions of the marine propeller. The MRF approach was utilized to investigate the flow around the marine propeller. Numerical analyses were carried out using only one blade passage because of the periodicity. The marine propeller was positioned at the center of the enclosed cylinder flow domain, and the distance between the propeller and the inlet of the domain was  $3D$ . Also, the distance between the propeller and the outlet of the domain was  $5D$ . The diameter of the fixed enclosed cylinder was adjusted to be  $5D$ , and the rotating domain diameter was  $0.72D$ . The study concluded that for the computational estimations of the marine rotor, hexa-structured and hybrid-unstructured meshes and the two different turbulence models exhibited similar accuracy levels. BSL-RSM achieved slightly more accurate numerical predictions compared to the SST turbulence model. Higher computational requirements and time were the disadvantages of the BSL-RSM turbulence model compared to the SST turbulence model. Therefore, the study stated that the SST turbulence model might be a more practical choice for a similar kind of numerical analysis.

In the numerical study of Wang and Walters [28] where they investigated the marine propeller performance using a transition-sensitive turbulence modeling, they exhibited a method to reduce the difference between experimental data (water-tunnel and open-water) and CFD results by performing the transitional analysis. They observed that the difference between computed thrust and torque with the regarding experimental data rose with increasing propeller load. This condition contributed to a large laminar flow region to occur on the propeller, so turbulence transition occurred with an increasing propeller load. This observation drew their attention to a transition-sensitive turbulence modeling study. Numerical predictions for incompressible flow around marine propeller P5168 were performed with an advance ratio ranging from 0.0 to 1.60. A transition-sensitive  $k-\omega$  eddy-viscosity turbulence model was applied to analyze the performance of the propeller by using Loci-CHEM flow solver. The study proposed that particularly with the increasing propeller load, the transition-sensitive

turbulence model presented better surface stresses, flow separations, and tip-vortex originations compared to the standard  $k-\omega$  SST turbulence model.

In another study on marine propellers, Benini [29] compared the performance results of the three different analysis methods available and discussed them. Firstly, the results of the combined momentum-blade element theory (CMBET) were validated according to the experimental test results. Then, fully three-dimensional RANS based numerical solution results were obtained by using the CFD analysis software ANSYS Fluent. Wageningen B3-50 propeller blade was positioned into the cylindrical flow domain, and this domain included nearly 800,000 nodes, 20,000 of which were generated on the propeller surface. For propeller performance analysis solution, the standard  $k-\varepsilon$  turbulence model was utilized. The study stated that the accuracy of propeller performance predictions was linked to advance ratio ( $J$ ) precisely, and a good agreement between the numerical method and experiments were acquired without being attached to  $J$ . As a result of the numerical analysis, a 5% maximum discrepancy was obtained compared with the experimental data. Besides, CMBET approach results were considerably reliable but not better than the numerical analysis.

Similarly, Seo et al. [30] conducted a CFD investigation to analyze ship propeller with ANSYS Fluent. They examined the effect of the flexible meshing techniques for the propeller performance with an advance ratio at the range of 0.1 to 0.9. Flow domain was separated into two domains, involving the stationary and rotating regions. Unstructured meshes were generated for sensitive curved surfaces, and for the rest of the domain, structured meshes generated. Marine propeller was positioned 10D propeller distant from the inlet into the center of the enclosed cylinder flow domain. The outlet of the domain was considered at 27D downstream from the center of the marine propeller. The diameter of the fixed enclosed cylinder was adjusted to be 20D, and the rotating domain diameter was adjusted to 1.2D. Sliding mesh method was implemented to the open water test simulations to achieve a propeller rotation effect. As a result of the computational results, a 4.67% maximum deviation of the thrust coefficient was obtained compared with the existing experimental data, and a 7.12%

maximum deviation of torque coefficient was obtained for corresponding experiments.

In the numerical study of Hong and Dong [31] where they investigated the circulation distribution of DTMD4119 and CSSRC TM0501 propeller by using ANSYS Fluent, they presented that the CFD simulations had excellent potential for the circulation analysis. The numerical domain was adjusted as an enclosed cylinder with a diameter which was co-axial with the propeller and with a diameter  $5D$ . The inlet was positioned  $5D$  distance upstream from the propeller, while the outlet was at  $10D$  downstream. 4.5 million mesh elements, most of which surrounded the propeller were formed, and the SST  $k-\omega$  turbulence model was selected. As a result of the numerical analysis, a 6% maximum discrepancy was found compared with the experimental data.

Similarly, Tian et al. [32] conducted a performance analysis study on a two-bladed vertical axis wind turbine. Two-dimensional transient numerical analyses were performed by using ANSYS Fluent. Rotation motion of the wind turbine blade implemented by utilizing a sliding mesh model, and the RNG  $k-\epsilon$  turbulence model was selected. Flow domain was divided into three subdomains: rotor domain, wake domain, and outer domain. For meshing, quadrilateral elements were generated to all domains, and the meshing of the rotor domain was more intense than the other domains. Wind turbine simulation domain has a dimension of  $18D \times 12D$ , while the wake domain has a dimension of  $6D \times 2D$ . Wind turbine blade was positioned in the middle, at a  $6D$  from the inlet boundary. As a result of the numerical analysis, a 5% maximum discrepancy was obtained when comparing with the experimental data, and investigation proved that the stated meshing method was reliable for accurate solutions.

Pan and Sahoo [33] carried out a RANS-method-based-numerical study on hydrodynamic performance of pump jet propulsor E779A by using ANSYS CFX software. Simulation results were compared with the existing experimental results. The jet propulsor was put into the center of the cylinder flow domain ( $11D$  in length

and  $5D$  in diameter), and the distance between the propulsor and the inlet of the domain was  $4D$ . Also, the distance between the propulsor and the outlet of the domain was  $6D$ . Flow domain was separated into three subdomains: rotor domain, stator domain, and external flow field domain. The only rotating domain was defined as the rotor domain.  $1.5 \times 10^6$  structured mesh grids were generated for the flow domain.  $7 \times 10^5$  of these grids were generated for rotor domain and  $4.5 \times 10^5$  for stationary stator domain. The sliding mesh approach was utilized to investigate the interactions between the rotor and stator domain. The SST  $k-\omega$  turbulence model was employed for different advance ratios. As a result of the numerical analysis, thrust and torque values were observed to be satisfactorily correlated (max numerical difference  $< 8\%$ ).

Similarly, Kutty and Rajendran [8] proposed a numerical prediction method to determine APC Slow Flyer 10x7 propeller performance under low Reynolds number conditions by using ANSYS Fluent CFD software. Flow domain was separated into two domains, involving the stationary and rotating regions. The propeller was put into the center of the  $8D$  cube stationary domain, and the distance between the propeller and the inlet/outlet of the domain was  $4D$ . For the rotating domain, a cylinder enclosure was chosen, and its dimensions were adjusted to  $1.1D$  and  $0.4D$ . CFD analyses were made with a fixed rotational speed of 3008 RPM by implementing the MRF model. Unstructured meshing grid resolution study was carried out for five grids with the numbers of cells ranging from  $0.38 \times 10^6$  to  $4 \times 10^6$ . Turbulence model independency study was performed by comparing the standard  $k-\varepsilon$ , standard  $k-\omega$ , and SST  $k-\omega$  turbulence models. All the mesh and model independency study revealed satisfactory results, with a numerical and experimental discrepancy less than 5%. As a result of the numerical method verification and validation study comparisons, standard  $k-\omega$  turbulence model and  $0.38 \times 10^6$  numbers of mesh grids were selected for the analyses. Their CFD results were in a good agreement with the experimental findings obtained by Brandt [15]. Thus, CFD can be a reliable analyzing method for propeller performance studies. In another study on propellers, Kutty et al. [34] extended their previous research to define the performance analysis of the slotted

designs of the APC Slow Flyer 10x7 propeller with constant blade slot design and width. New slotted propellers, designed with seven different slot locations, analyzed in terms of thrust coefficient, power coefficient, and efficiency by utilizing the same computational setup settings of the previous study. Slotted designs resulted in a thrust increase from 0.1% to 4.75% and also a power coefficient increase from 10.38% to 44.59% for low advance ratios.

In the computational study of Chen et al. [35], propeller slipstream interaction on High Altitude Long Endurance (HALE) UAV was analyzed. Computational analyses were made using the MRF model to examine the accuracy of the MRF model. The flow field of the MRF model was in satisfactory agreement with the exact propeller flow. Analyses were made with and without propeller slipstream interaction of the UAV model for take-off, climbing, and cruising flight conditions. As a result of the study, it was proposed that the MRF model reliably presented the slipstream effect.

In their CFD study, Sunan [36] defined aerodynamic behaviors of a photography quadrotor by using ANSYS Fluent software. Lift, drag, and thrust forces on the quadrotor were specified by implementing over 20 CFD analyses for both steady and unsteady flow conditions. In this study, two different stationary flow domains and various solver settings were combined to assess their influence on the results. Figure 1.6a shows the quadrotor model with APC Slow Flyer 10x4.7 propellers in the quarter cylinder control volume. Flow domain was modeled as a quarter cylinder because each of the arms and propellers were identical. Boundary conditions and distances of the control volume consisting of rotating and stationary subdomains are shown in Figure 1.6b. Analyses were simulated with the MRF method and the SIMPLE algorithm. The distance between the propeller and the inlet of the domain was 20D for long and 4D for short domain. In addition, the distance between the propeller and the outlet of the domain was 36D for long and 12D for short domain (Figure 1.6b). Rotating domain diameter was adjusted to 1.1D. The prismatic mesh type was selected, and an equal number of mesh grids were generated for both long and short domains to investigate the effect of the cell size. As a result of the study, different simulation combinations

were tabulated and compared with the experimental study of Brandt [15]. One of the short domain results was found as the most accurate one.

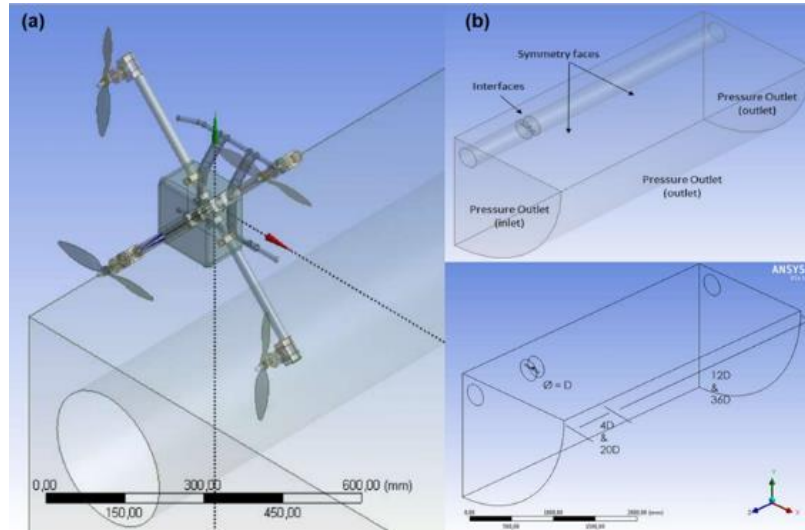


Figure 1.6. (a) Quadrotor simulation domain, (b) Boundary conditions, and distances of the control volume [36]

## 1.2. Previous Studies on Rotor Frame-arm

Rotor-rotor and rotor-airframe aerodynamic interactions are essential parameters in the performance of small-scale UAVs. Fernandes [37] designed and constructed Slim-arm (Figure 1.7d) and U-arm (Figure 1.7e) shapes for a quadrotor. The influence of these arm shapes on the performance of the quadrotor was evaluated by performing experiments. Both arm shapes had a small influence on the quadrotor performance, and as a result of the study, U-arm was chosen for the quadrotor. Similarly to Fernandes's study [37], Theys et al. [38] also investigated the influence of the propeller configuration, shape and dimension of the propeller arm on the rotor aerodynamic performance experimentally. Three different type of arm shapes (cylinder (Figure 1.7a), aerodynamic geometry (Figure 1.7b), and square (Figure 1.7c)) were tested, and they showed that the square shape was the best design due to having the better propulsive efficiency in hovering flight. Both Fernandes [37], and

Theys et al. [38] experimentally performed their arm shape study to enhance the propulsive efficiency.

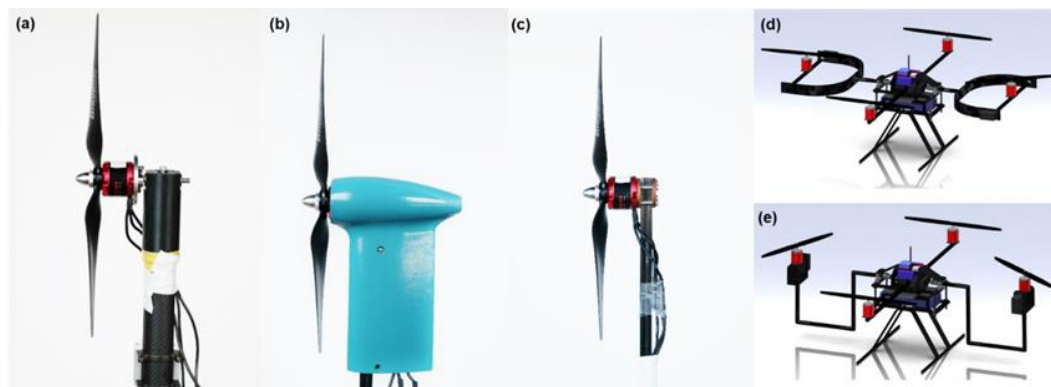


Figure 1.7. (a) 25mm tube, (b) nacelle, (c) 10mm square tube [38], (d) Slim-arm model, (e) U-arm model [37]

Unlike Fernandes [37] and Theys et al. [38], Penkov and Aleksandrov [39] performed experiments and numerical analysis to investigate rotor-rotor interactions, and they compared the results from experiments and CFD simulations. Eventually, they came up to an optimal distance between rotors. Evidently, CFD simulations are employed to a better understanding of rotor-rotor and rotor-airframe aerodynamic interactions. In addition to this, new designs can be evaluated accurately in any situation in a less time-consuming way. In this sense, the present work focuses on rotary-wing aerodynamics in order to evaluate the interaction between propellers and rotor arm.

### 1.3. Aim and Structure of the Thesis

It is clearly seen from the previous studies that the rotary-wing aerodynamics is still a goal of ongoing research to reach the most efficient quadrotor performance. While experimental studies mostly focus on measurements of rotor aerodynamics, numerical methods enable more complex situations to be simulated. However, there are limited experimental and numerical studies on the effects of different rotor frame arm geometries.

The objective of this study is to investigate the interaction between propellers and rotor frame arm of different geometries in hovering flight and to assess the influence of the frame arm on the aerodynamic performance of the rotor. In the first step, a dedicated experimental investigation has been performed on a 16-inch propeller at different flight regimes for the various rotational speeds of the propeller. Simultaneous torque and thrust measurements were made, and the results were compared with the numerical simulations performed in ANSYS Fluent. In the second step, four different arm shapes (i.e., Eppler Arm, 25mm cylindrical tube, 25mm square tube, and 25mm square tube with a 10mm slot) were included in the numerical flow solutions for the 16-inch propeller in order to assess their influence on the aerodynamic rotor performance.

This thesis consists of five chapters. In this Chapter, the literature survey on the aerodynamic performance of quadrotor propellers and rotor frame arm was explained. In Chapter 2, experimental methodology and setup regarding the propeller test instruments and its design are explained. In Chapter 3, numerical methodology for the propeller and different arm shapes are defined. The mesh and model independency studies are presented for vertical climb and hovering flight configurations. In Chapter 4, experimental and numerical study results are discussed and evaluated. Finally, major conclusions and future works are given in Chapter 5.



## CHAPTER 2

### EXPERIMENTAL SETUP AND METHODOLOGY

In this chapter, the aerodynamic performance measurements of the propellers considered in this study will be addressed. In the first part, the wind tunnel facility used in the current study will be identified in detail. Subsequently, experimental setup, testing procedure, and data reduction and validation will be described for different motion kinematics and associated terms.

#### 2.1. Wind Tunnel Facility

The thrust and torque measurements were performed in the test section of low-speed METUWIND C3 wind tunnel at the Rüzgem (Metuwind) - Center for Wind Energy Research (Figure 2.1). The wind tunnel is a medium scale suction type which is powered by a 45-kW speed controlled electrical motor connected to an axial fan. The wind tunnel has a Plexi-Glass transparent test section and contains a 2D contraction section with an area ratio of 1:5. Honeycombs and screens are used to maintain good flow quality in the wind tunnel. Wind speed in the test-section is variable up to 25 m/s, and the turbulence intensity is less than 1% [40]. For the measurements conducted in this study, the maximum tunnel speed used was 5.42 m/sec.



Figure 2.1. METUWIND C3 wind tunnel

## 2.2. Experimental Setup

In order to acquire the performance characteristics, it is necessary to measure the thrust, torque, angular velocity, and freestream flow conditions. These mentioned values were measured successfully with the experiments conducted for the current study. The test setup consists of test equipment, measurement devices, and data acquisition system. The test equipment (wind tunnel, mechanical structure, brushless motor, and propeller), measurement devices (force, moment, velocity, temperature, and pressure), and the data acquisition system (computer, power supply, data acquisition board, and related software) of the current study will be introduced in the following section.

Two different propellers, APC Slow Flyer 11x4.7 propeller and 16x4 carbon fiber propeller were used in this study. The APC Slow Flyer 11x4.7 propeller (Figure 2.2a), was used for the validation of the experimental setup that is utilized for thrust and torque measurements. The 16x4 carbon fiber propeller (Figure 2.2b), was the primary experimental model used in this study following with numerical analysis.

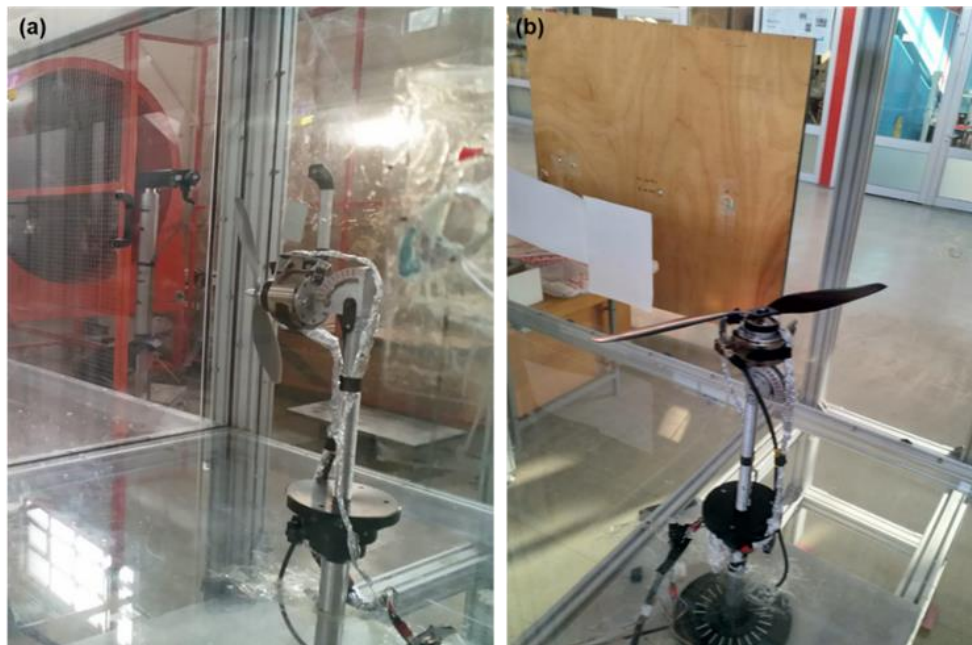


Figure 2.2. Experimental setup with (a) APC Slow Flyer 11x4.7 and (b) Carbon fiber 16x4 propeller

Dwyer Model 471B Thermo-Anemometer, which measures air velocity or air volume and temperature simultaneously, is utilized to measure free stream velocity (Figure 2.3a). Its range for the air velocity is from 0 to 30 m/s, and for the temperature is from  $-40$  to  $100^{\circ}\text{C} \pm 0.28^{\circ}\text{C}$ . The atmospheric pressure outside of the wind tunnel is simultaneously measured with an Extech SD700 barometric pressure/humidity/temperature datalogger (Figure 2.3b). Its range for the barometric pressure is 10 to 1100 hPa, and the temperature is  $0$  to  $50^{\circ}\text{C} \pm 0.8^{\circ}\text{C}$ .

The ATI Gamma SI-32-2.5 Multi-Axis Force/Torque Sensor system was used to measure all six force and moment components (Figure 2.4a). The Quantum MT Series 4108 370KV brushless multirotor motor (Figure 2.4b), the load cell, and the propeller were mounted to a mechanical structure, which was designed and manufactured by Kaya [22]. In the next step, the whole structure was placed in the test section of the wind tunnel to measure forces and torques simultaneously.

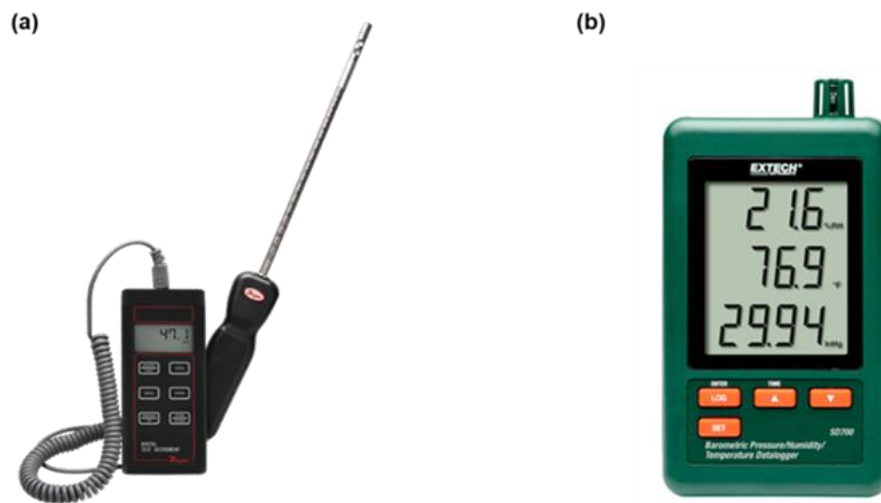


Figure 2.3. (a) Dwyer Model 471B thermo-anemometer [41], (b) Extech SD700 barometric pressure/humidity/temperature data logger [42]

In Figure 2.2, where the setup is shown, the general design consists of a mechanical structure support that was installed into the wind tunnel from the bottom wall of the test section is presented. In the experimental setup, the ATI Gamma load cell was positioned between the brushless motor and the mechanical structure. Thus, the

aerodynamic loads affecting the mechanical structure were not measured by the ATI Gamma load cell. The Quantum brushless motor was adjusted to run with a speed controller. Angular velocity of the propellers was observed with an optical RPM sensor, and the Eagle Tree eLogger software was used to set the rotational speed. To calculate the propeller speed, the velocity sensor was focused at the motor which has a white strip of tape. A photograph of the RPM sensor mounted on the test rig is shown in Figure 2.4c.



Figure 2.4. (a) ATI Gamma loadcell [22], (b) Quantum brushless motor, (c) RPM sensor with the test setup

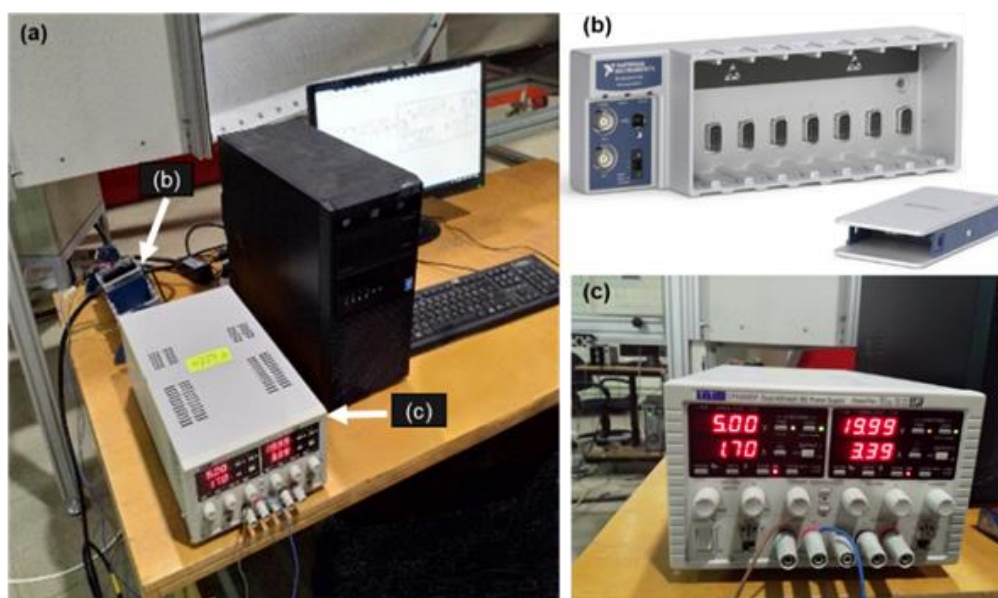


Figure 2.5. (a) Data acquisition setup, (b) NI Compact DAQ-9178 data acquisition chassis [43], (c) DC power supply

The National Instruments, NI Compact DAQ-9178 data acquisition platform (Figure 2.5b) was utilized to record testing equipment voltages to the computer. The National Instruments LABVIEW programming software was employed to read, manage, and monitor the progress of the experiment from the DAQ platform (Figure 2.5a). Thrust and torque measurements were performed at the data acquisition frequency of 1000 Hz. An external laboratory DC power supply was utilized to operate the brushless motor of the propeller at a voltage difference of 5.0 V. (Figure 2.5c).

### **2.3. Testing Procedure**

The primary purpose of the experimental part of the study was to measure the thrust and moment forces of the propeller for hovering and vertical climb flight configurations. The test equipment mentioned in the previous part, measurement devices, and data acquisition system were used to achieve experimental tests. Calibration checks were applied regularly to maintain consistent results. In hovering flight tests, free stream velocity was zero, so only the rotational speed of the propeller was measured at different RPM values. In vertical climb flight tests, both the rotational speed of the propeller and the free stream velocity were measured and set to desired values. The following steps were applied while conducting the measurement tests.

- a. Mechanical structure support installed into the bottom of the wind tunnel, and after installation, the gaps were sealed with tape.
- b. Load cell, brushless motor, and the test propeller were assembled to the mechanical structure.
- c. Data acquisition system, computer, and power supply were connected to test equipment and measurement devices.
- d. LabVIEW and the Eagle Tree eLogger software were opened as ready to use on the computer.
- e. The power supply was turned on and checked (Beep sound of the motor was heard.). Then it was adjusted to the test.
- f. Servo tester was checked (A trial run was started for the propeller.).

- g. For vertical flight test, the wind tunnel was set to the desired speed, and free stream velocity was checked with the portable hotwire anemometer.
- h. Ambient pressure and temperature were recorded during each run.
- i. The measurement process was biased before every single test. Thrust and moment data were recorded 15 seconds before the start of the test; the recording was continued for 15 seconds after the end of the test.
- j. For both hovering and vertical climb tests, the rotational speed of the propeller was regulated with the knob on the servo tester till the desired rotational speed was read from Eagle Tree eLogger software.
- k. Collected thrust and moment data were recorded with LabVIEW.
- l. The experiment was terminated by performing the above operations in the reverse order.

Thrust and torque were measured for the vertical climb and hovering flight at various rotor speeds and free stream velocities. Each test was repeated three times for both propellers and flight conditions. The measurement matrix is tabulated below in Table 2.1. For APC Slow Flyer 11x4.7 propeller, hovering flight test measurements were obtained at 2556, 3423, 4290 and 5175 RPM values. For 16inch carbon fiber propeller, hovering flight performance tests were conducted at 1050, 2000, and 3150 RPM values.

In order to perform vertical climb flight performance tests, APC Slow Flyer 11x4.7 propeller RPM was set to 3004 and 4003, and the tunnel speed was adjusted to 4.91, 6.14 and 8.03m/s. Also, the 16-inch carbon fiber propeller RPM was set to 2000 and 3150, and the tunnel speed was arranged to 3.42 and 5.42 m/s for vertical climb flight performance tests.

Table 2.1. Thrust and Torque measurement conditions

	Hovering Flight Tests	Vertical Climb Flight Tests	
Propeller Type	Rotational speed of the propeller(RPM)	Rotational speed of the propeller(RPM)	Free Stream Velocity (m/s)
APC Slow Flyer 11x4.7	2556, 3423, 4290 and 5175	3004 and 4003	4.91, 6.14 and 8.03
Carbon Fiber 16x4	1050, 2000 and 3150	2000 and 3150	3.42 and 5.42

#### 2.4. Data Reduction and Validation

As mentioned in the experimental setup section, thrust and torque data acquisition were carried out by utilizing the multi-axis load cell that converts voltage measurements to the physical values. The rotational speed of the propeller, free stream velocity, ambient pressure, and temperature were measured with proper measurement devices (see section 2.2). From these measurements, air density is calculated according to the equation of state (Equation 2.1).

$$\rho = \frac{P_{atm}}{RT_{air}} \quad (2.1)$$

The propeller power can be calculated from Equation 2.2.

$$P = 2\pi nQ \quad (2.2)$$

Propeller measurements and calculations are non-dimensionalized to acquire the performance data. The power and thrust coefficient equations are shown below (Equation 2.3 and Equation 2.4).

$$C_P = \frac{P}{\rho n^3 D^5} \quad (2.3)$$

$$C_T = \frac{T}{\rho n^2 D^4} \quad (2.4)$$

$$J = \frac{V}{nD} \quad (2.5)$$

In these equations,  $T$  (N) is the thrust produced by propeller,  $Q$  (Nm) is torque,  $\rho$  (kg/m<sup>3</sup>) is the density of the fluid,  $V$  (m/s) is the free stream velocity,  $D$  (m) is the diameter of the propeller and  $n$  (rps) is the rotational speed of the propeller. For vertical climb flight conditions, the advance ratio can be described as the ratio of velocity and the rotation rate (Equation 2.5). For hovering flight conditions,  $J$  becomes zero (because of  $V=0$ ).

In order to validate the test data, uncertainty analysis, repeatability of the tests, and comparison of APC Slow Flyer 11x4.7 propeller measurements between the results of METU and UIUC were performed. The validation approaches will be explained in the following sections.

#### 2.4.1. Uncertainty analysis

A general uncertainty analysis is carried out by utilizing the standard uncertainty distribution method. The reported thrust and torque values are the time-average of 10,000 data points captured during the operation of the propeller. The uncertainty was estimated according to the method shown in Coleman & Steele [6] (Equation 2.6).

$$\hat{V} = \bar{M} \pm U \quad (2.6)$$

where,  $\hat{V}$  is the estimated value,  $\bar{M}$  is the measured mean value of thrust or torque, and  $U$  is the expanded uncertainty.

$$\hat{V} = \bar{M} \pm \frac{k\sigma}{\sqrt{N}} \quad (2.7)$$

In Equation 2.7,  $\sigma$  is the measured standard deviation,  $k$  is the coverage factor, and  $N$  is the number of samples. Calculation of the  $\bar{M}$  and  $\sigma$  is shown in Equation 2.8.

$$\bar{M} = \frac{1}{N} \sum_{i=1}^N M_i, \sigma = \left[ \frac{1}{N-1} \sum_{i=1}^N (M_i - \bar{M})^2 \right]^{1/2} \quad (2.8)$$

A summary of the estimated thrust and torque uncertainty analysis values is given in Table 2.2 for APC Slow Flyer 11x4.7 propeller. The reported expanded uncertainty is based on a standard uncertainty ( $u = \sigma/\sqrt{N}$ ) multiplied by a coverage factor  $k = 1.96$ , providing a level of confidence of approximately 95%.

Table 2.2. Thrust and Torque uncertainty estimates

APC Slow Flyer 11x4.7	Hovering Flight Tests	Vertical Climb Flight Tests	
	Rotational speed of the propeller (RPM)	Rotational speed of the propeller (RPM)	Free Stream Velocity (m/s)
	4290	4003	4.92
Thrust	0.221%	0.625%	
Torque	0.555%	0.597%	

Observing several data sets revealed that the uncertainty in the thrust and torque measurements all prove to be small. And the uncertainty analysis results were consistent with the study of Brandt and Selig [15].

#### 2.4.2. Repeatability of the test measurements

The test setup consisting test equipment, measurement devices, and a data acquisition system must supply consistent data whenever it is obtained. In order to analyze test data accurately, each test is repeated three times for both propellers and flight conditions. It was seen that propeller test measurement results matched one another well, and repeatability was attainable for both propellers and flight conditions.

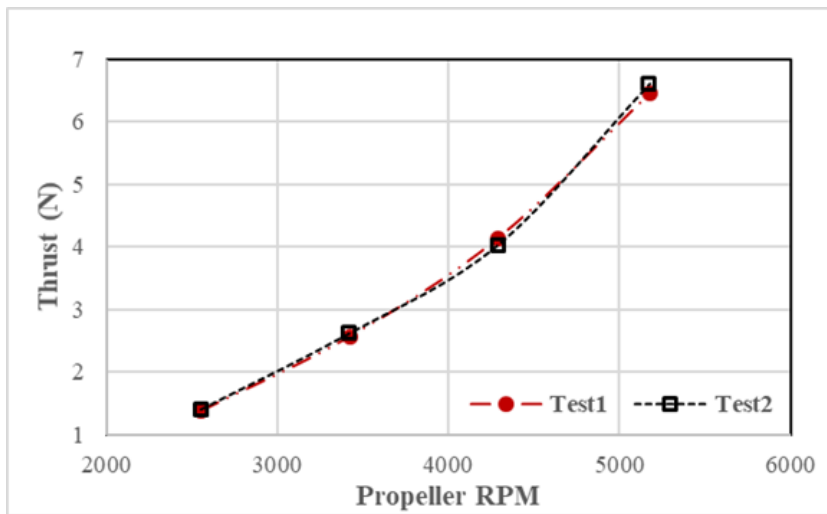


Figure 2.6. Thrust repeatability data for APC Slow Flyer 11x4.7 propeller for hovering flight

Figure 2.6 and Figure 2.7 present the comparisons of the APC Slow Flyer 11x4.7 propeller hovering flight performance results obtained from two different tests under the same conditions. Hovering flight thrust and torque values versus the corresponding RPMs are plotted in the figures for hovering flight.

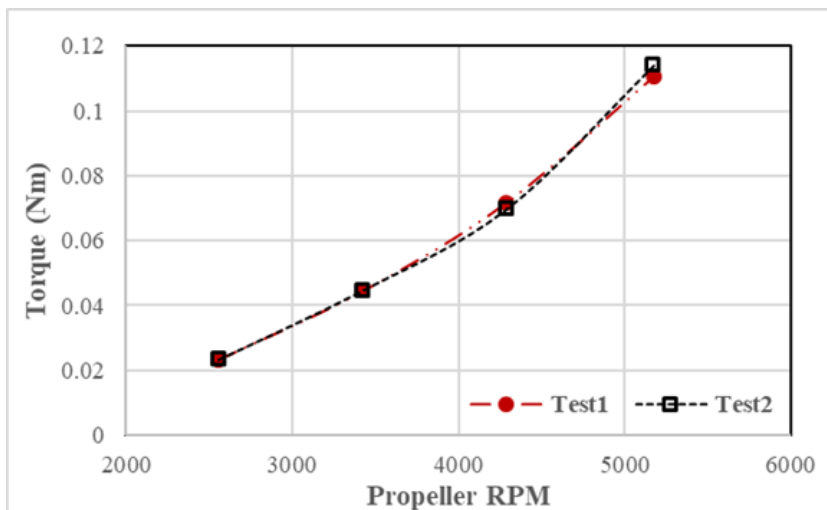


Figure 2.7. Torque repeatability data for APC Slow Flyer 11x4.7 propeller for hovering flight

Vertical climb flight performance result comparisons of the APC Slow Flyer 11x4.7 propeller are shown in Figure 2.8 and Figure 2.9. Vertical climb flight thrust and

power coefficients versus the corresponding advance values are shown in figures for vertical climb flight.

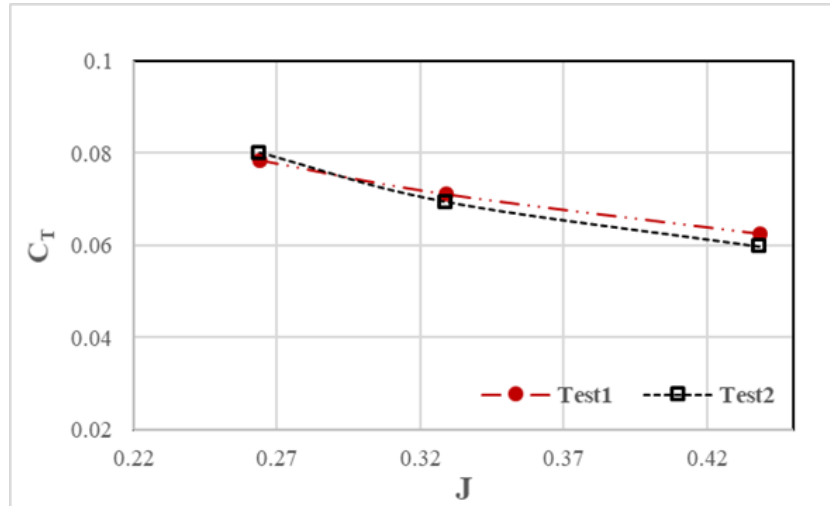


Figure 2.8. Thrust coefficient repeatability data for APC Slow Flyer 11x4.7 propeller for vertical climb flight

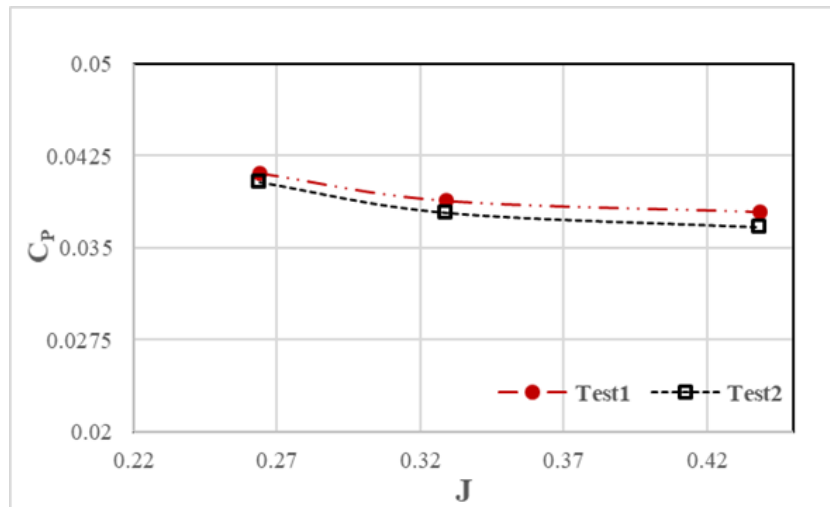


Figure 2.9. Power coefficient repeatability data for APC Slow Flyer 11x4.7 propeller for vertical climb flight

### 2.4.3. Comparison of propeller measurements

Another way to validate the test data is comparing the data with other tests. The measured thrust and torque values at different RPM settings both in hovering and in

vertical climb flight configurations were compared to the experimental data reported by Brandt [15]. The measurement procedure used in this study was different from the measurement technique of Brandt. For the current study, Multi-Axis Force/Torque Sensor system was connected directly to the brushless motor to gather data (Figure 2.4c). For the study of Brandt, the torque was measured with a torque cell connected to the motor housing into the wind tunnel (Figure 1.5b) and thrust with a load cell connected to a pivot arm that was placed outside of the tunnel (Figure 1.5a). As a result of the hovering flight test comparison study, when compared with the relevant experimental data of Brandt, a maximum discrepancy of 5.65% for thrust coefficient and 5.97% for power coefficient was obtained. Investigation proved that the applied testing method was reliable for other conducted tests of the current study. Figure 2.10 and Figure 2.11 show the comparisons of the APC Slow Flyer 11x4.7 propeller hovering flight performance results obtained from two different facilities with different measurement techniques. Hovering flight thrust and power coefficients versus the corresponding RPMs are shown in figures for hovering flight.

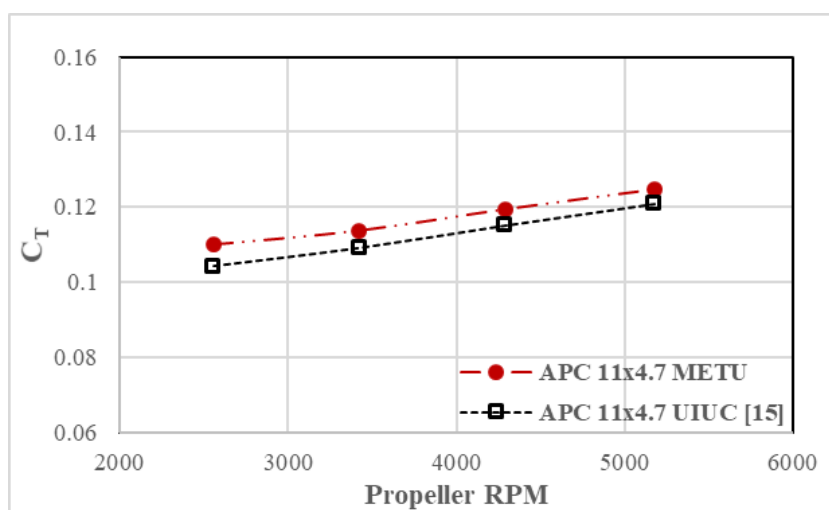


Figure 2.10. Thrust coefficient comparison data for APC Slow Flyer 11x4.7 propeller for hovering flight

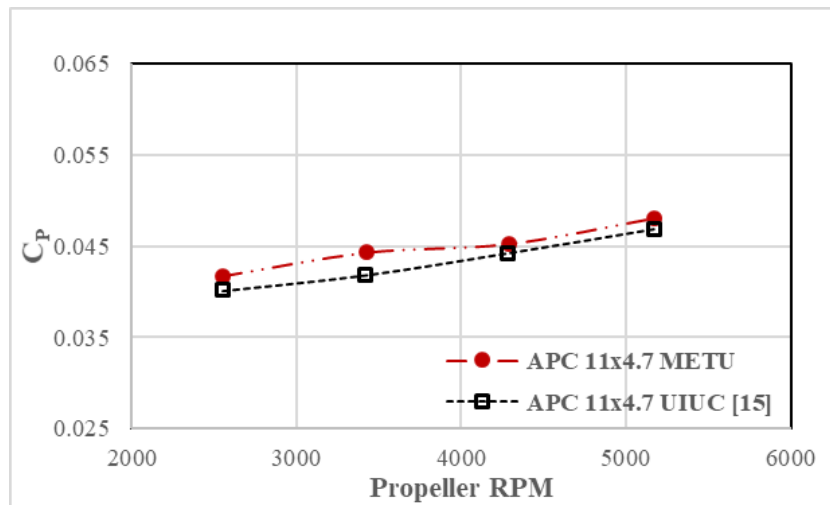


Figure 2.11. Power coefficient comparison data for APC Slow Flyer 11x4.7 propeller for hovering flight

METU and UIUC propeller performance comparison data presented in Figure 2.10 and Figure 2.11 are shown in Table 2.3. The values of  $C_T$  and  $C_P$  are given in the table, and the difference between them is demonstrated as a percentage.

Table 2.3. Thrust and Power coefficient comparison data for hovering flight

APC Slow Flyer 11x4.7						
	UIUC		METU		Comparison	
RPM	$C_T$	$C_P$	$C_T$	$C_P$	$C_T$ Difference	$C_P$ Difference
2556	0.1042	0.0401	0.1100	0.0417	5.65%	4.00%
3423	0.1091	0.0418	0.1138	0.0442	4.31%	5.97%
4290	0.1151	0.0442	0.1194	0.0452	3.79%	2.39%
5175	0.1209	0.0468	0.1247	0.0480	3.17%	2.76%

As a result of the vertical climb flight test comparison between two studies, a maximum inconsistency of 8.46% for the thrust coefficient and 6.08% for the power coefficient was obtained. Thus, comparison study has proven that the test method is

reliable for further tests of this study. Vertical climb flight performance results comparison of the APC Slow Flyer 11x4.7 propeller is given in Figure 2.12 and Figure 2.13. Vertical climb flight thrust and power coefficients versus the corresponding advance ratio values are shown in figures for vertical climb flight.

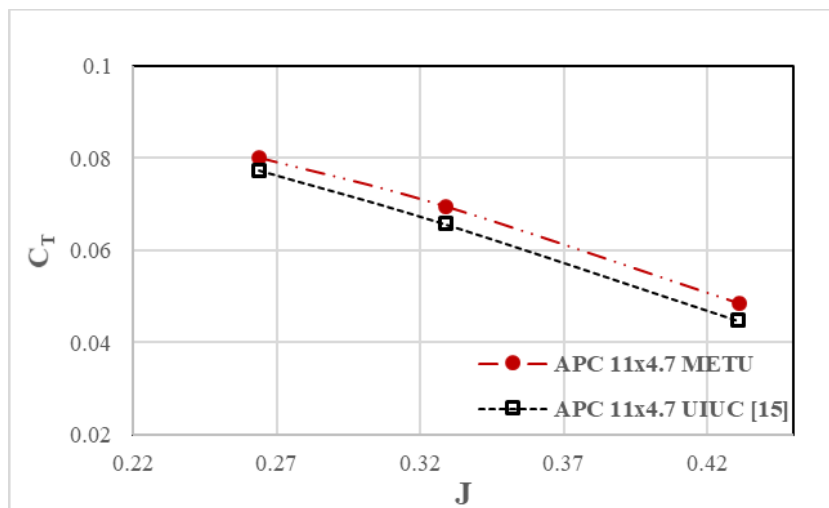


Figure 2.12. Thrust coefficient comparison data for APC Slow Flyer 11x4.7 propeller for vertical climb flight

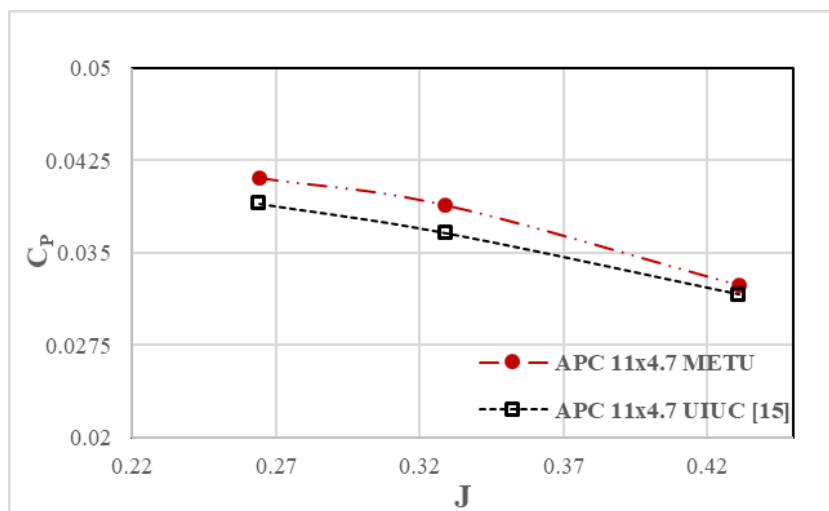


Figure 2.13. Power coefficient comparison data for APC Slow Flyer 11x4.7 propeller for vertical climb flight

METU and UIUC propeller performance comparison data presented in Figure 2.12 and Figure 2.13 are shown in Table 2.4. The values of  $C_T$  and  $C_P$  are represented in the table, and the difference between them is indicated as a percentage.

Table 2.4. Thrust and Power coefficient comparison data for vertical climb flight

APC Slow Flyer 11x4.7								
			UIUC		METU		Comparison	
RPM	J	v	$C_T$	$C_P$	$C_T$	$C_P$	$C_T$ Difference	$C_P$ Difference
4003	0.264	4.92	0.0773	0.0390	0.0799	0.0410	3.46%	5.25%
4003	0.329	6.13	0.0656	0.0366	0.0694	0.0388	5.85%	6.08%
4003	0.431	8.03	0.0447	0.0316	0.0484	0.0323	8.46%	2.30%

The reasons for the differences between the results of the two studies may be due to the loadcell accuracy, fluctuations in free-stream velocity, or improper positioning of the propeller, motor, and mechanical structure. As a result of three mentioned validation approaches, the current study presents reliable test data. Thus, a proper comparison for experimental and numerical analysis for 16-inch carbon fiber propeller is possible. In the next chapter, the numerical analysis of 16-inch carbon fiber propeller will be presented.



## CHAPTER 3

### NUMERICAL ANALYSIS AND METHODOLOGY

In this chapter, the methodology of the aerodynamic performance measurements of the propellers, which were simulated with the ANSYS Fluent CFD solver software, will be addressed. First, the underlying theory of CFD software will be briefly summarized. Afterwards, the numerical methodology for the propeller and different arm shapes will be defined in detail. Finally, mesh and model independency studies will be described for vertical climb and hovering flight configurations.

#### 3.1. Computational Fluid Mechanics Differential Equations

##### 3.1.1. Continuity equation

The continuity equation derived for incompressible flows that defines the conservation of mass in a control volume (Equation 3.1) is as follows:

$$\nabla \cdot (\vec{V}) = 0 \quad (3.1)$$

where  $\vec{V}$  is absolute velocity.

##### 3.1.2. Momentum conservation equations

Conservation of momentum in an inertial reference frame is defined as follows in Equation 3.2.

$$\nabla \cdot (\vec{V} \cdot \vec{V}) = -\frac{1}{\rho} \nabla p + \frac{1}{\rho} \nabla \cdot \bar{\tau} - 2\vec{\Omega} \times \vec{V} - \frac{1}{\rho} \vec{\Omega} \times (\vec{\Omega} \times \vec{r}) \quad (3.2)$$

where  $p$  is the static pressure,  $\bar{\tau}$  is the stress tensor,  $\vec{\Omega}$  is the rotational speed vector,  $\vec{r}$  is the radius of cell center from the rotation axis. In equation 3.2,  $2\vec{\Omega} \times \vec{V}$  term is the coriolis acceleration, and  $\vec{\Omega} \times (\vec{\Omega} \times \vec{r})$  is centrifugal force produced by rotation. Last

two terms are moving reference frame terms for rotational reference frame that is used to simulate the rotation of propeller.

$$\bar{\tau} = (\mu + \mu_t)[(\nabla\vec{V} + \nabla\vec{V}^T)] \quad (3.3)$$

The stress tensor is described in Equation 3.4, where  $\mu$  is the molecular viscosity and  $\mu_t$  is the turbulent viscosity. Volumetric dilation term does not exist for incompressible flows.

### 3.1.3. Turbulence modeling

Turbulence modeling is the construction and usage of a mathematical model to estimate the effects of turbulence that is a crucial point in most CFD simulations. Almost all engineering problems are turbulent, and therefore require a turbulence model. Turbulence modeling strategies have been developing as computing power increases, and for that reason, turbulence modeling is a continuous process. A variety of methods are developed to model turbulent flows. The most commonly used turbulence models are listed in the following section:

- Reynolds-Averaged Navier-Stokes (RANS)
- Direct Numerical Simulation (DNS)
- Detached Eddy Simulation (DES)
- Large Eddy Simulation (LES)

Choosing the appropriate method to model turbulence physics is crucial. In this study, RANS-based turbulence models were utilized for investigating the fluid motion. The turbulence models for the RANS equations aim to calculate the Reynolds stresses. Reynolds stresses can be calculated in the following three subcategories:

- Linear eddy viscosity models
- Nonlinear eddy viscosity models
- Reynolds stress model (RSM)

Linear eddy viscosity models are formed by a linear constitutive relationship (Equation 3.4) with the mean flow straining field (Boussinesq Hypothesis),

$$-\rho\langle u_i u_j \rangle = 2\mu_t S_{ij} - \frac{2}{3} \rho k \delta_{ij} \quad (3.4)$$

where  $\mu_t$  is the turbulence viscosity or eddy viscosity, and  $\delta$  is the Kronecker delta function. Moreover, the mean turbulent kinetic energy is defined in Equation 3.6.

$$\langle u_1 u_1 \rangle = \langle u_2 u_2 \rangle = \langle u_3 u_3 \rangle \quad (\text{isotropic assumption}) \quad (3.5)$$

For the k- $\omega$  turbulence model, turbulence stresses are isotropic (not dependent to the direction vector) Equation 3.5.

$$k = \frac{1}{2} (\langle u_1 u_1 \rangle + \langle u_2 u_2 \rangle + \langle u_3 u_3 \rangle) = \frac{3}{2} \langle u_1 u_1 \rangle \quad (3.6)$$

Mean strain rate is given in Equation 3.7.

$$S_{ij} = \frac{1}{2} \left[ \frac{\partial u_i}{\partial x_j} + \frac{\partial u_j}{\partial x_i} \right] - \frac{1}{3} \frac{\partial u_k}{\partial x_k} \delta_{ij} \quad (3.7)$$

There are three main categories for the linear eddy viscosity models. These categories are listed below and specified by the number of equations solved to calculate the vortex viscosity coefficient.

- Algebraic models
- One equation models
- Two equation models

Two equation turbulence models like k- $\epsilon$  and k- $\omega$  models are widely used in most engineering problems, and are still an active research subject that has been developing. The two equations turbulence models propose a relatively low-cost computation that are applicable to model general turbulent flows. The k- $\omega$  model utilizes two additional transport equations to model turbulence properties. In k- $\omega$  model, k variable is the turbulent kinetic energy, and the second transported  $\omega$  variable stands for the specific dissipation. Here, k and  $\omega$  variables identify the energy in the turbulence and scale of

the turbulence (length or time), respectively.  $k$  and  $\omega$  variables are acquired from the following transport equations (Equation 3.8 and Equation 3.9):

$$\frac{\partial}{\partial x_i} (k u_i) = \frac{1}{\rho} \frac{\partial}{\partial x_j} \left( \left( \mu + \frac{a_\infty^* \rho k}{\sigma_k \omega} \left( \frac{\beta_i + \frac{\rho k}{\mu \omega R_k}}{1 + \frac{\rho k}{\mu \omega R_k}} \right) \right) \frac{\partial k}{\partial x_j} \right) + \frac{a_\infty^* S^2 k}{\omega} \left( \frac{\beta_i + \frac{\rho k}{\mu \omega R_k}}{1 + \frac{\rho k}{\mu \omega R_k}} \right) - \beta_\infty^* f_{\beta^*} k \omega \left( \frac{\frac{4}{15} + \left( \frac{\rho k}{\mu \omega R_\beta} \right)^4}{1 + \left( \frac{\rho k}{\mu \omega R_\beta} \right)^4} \right) \quad (3.8)$$

$$\frac{\partial}{\partial x_i} (\omega u_i) = \frac{1}{\rho} \frac{\partial}{\partial x_j} \left( \left( \mu + \frac{a_\infty^* \rho k}{\sigma_\omega \omega} \left( \frac{\beta_i + \frac{\rho k}{\mu \omega R_k}}{1 + \frac{\rho k}{\mu \omega R_k}} \right) \right) \frac{\partial \omega}{\partial x_j} \right) + \frac{S^2 a_\infty \left( a_0 + \frac{\rho k}{\mu \omega R_\omega} \right)}{1 + \frac{\rho k}{\mu \omega R_\omega}} - \frac{\beta_i \omega^2 \left( 1 + 70 \left| \frac{\Omega_{ij} \Omega_{jk} S_{ki}}{(\beta_\infty^* \omega)^3} \right| \right)}{1 + 80 \left| \frac{\Omega_{ij} \Omega_{jk} S_{ki}}{(\beta_\infty^* \omega)^3} \right|} \quad (3.9)$$

In these equations, effective diffusivity of  $\omega$  and  $k$  are included to the first terms. Second term in Equation 3.8 defines the production of turbulence kinetic energy as a result of mean velocity gradients. Second term in Equation 3.9 defines the generation of  $\omega$ . Third term in Equation 3.8 and Equation 3.9 shows the dissipation of  $k$  and  $\omega$  as a result of the turbulence.  $\sigma_k$  and  $\sigma_\omega$  are the turbulent Prandtl numbers for  $k$  and  $\omega$ , respectively.  $S$  is the modulus of the mean rate-of-strain tensor.

where  $f_{\beta^*}$  is (used while computing dissipation of  $k$ ) (Equation 3.10)

$$f_{\beta^*} = \begin{cases} 1, & \frac{1}{\omega^3} \frac{\partial k}{\partial x_j} \frac{\partial \omega}{\partial x_j} \leq 0 \\ \frac{1 + 680 \left( \frac{1}{\omega^3} \frac{\partial k}{\partial x_j} \frac{\partial \omega}{\partial x_j} \right)^2}{1 + 400 \left( \frac{1}{\omega^3} \frac{\partial k}{\partial x_j} \frac{\partial \omega}{\partial x_j} \right)^2}, & \frac{1}{\omega^3} \frac{\partial k}{\partial x_j} \frac{\partial \omega}{\partial x_j} > 0 \end{cases} \quad (3.10)$$

Rotation rate  $\Omega_{ij}$  is defined in Equation 3.11 (used while computing dissipation of  $\omega$ )

$$\Omega_{ij} = \frac{1}{2} \left( \frac{\partial u_i}{\partial x_j} - \frac{\partial u_j}{\partial x_i} \right) \quad (3.11)$$

Model constants utilized in Equation 3.8 and Equation 3.9 are presented in the following section.

$$a_{\infty}^* = 1, a_{\infty} = 0.52, a_0 = \frac{1}{9}, \beta_{\infty}^* = 0.09, \beta_i = 0.072, R_{\beta} = 8$$

$$R_k = 6, R_{\omega} = 2.95, \zeta^* = 1.5, M_{t0} = 0.25, \sigma_k = 2.0, \sigma_{\omega} = 2.0$$

When the turbulence equations are solved near the wall, the wall effects need to be modeled. These effects are modeled by separating them into laminar sub-layer, buffer layer and fully turbulent layer [44]. The wall function (Equation 3.12), which is utilized in the laminar sub-layer, was used in the current study to make high precision modeling. In order to perform accurate analysis in this region, the cell structure was formed such that  $y^+$  was less than one. However, for correct solutions, this value can be less than five. In this function, the dimensionless wall velocity ( $u^+$ ) is the function of the  $y^+$ . The  $u^+$  and  $y^+$  are given in Equation 3.13 and Equation 3.14, respectively.

$$u^+ = y^+ \quad (3.12)$$

$$u^+ = \frac{u}{\sqrt{\tau_w/\rho}} \quad (3.13)$$

In these equations,  $u$  is the velocity of the cell next to the wall,  $\tau_w$  is the shear stress at the wall, and  $y$  is the distance of the wall.

$$y^+ = \frac{y\sqrt{\tau_w/\rho}}{\nu} \quad (3.14)$$

## 3.2. CFD Modelling Methodology

### 3.2.1. Simulation approach

Nowadays, a considerable amount of freeware and commercial CFD codes are available. Commercially available CFD solver ANSYS Inc. Fluent 17 was used for numerical solutions of the current study. The process of obtaining results with the CFD software took place in three phases, which are pre-processor, solver, and post-processor [36] (Figure 3.1).

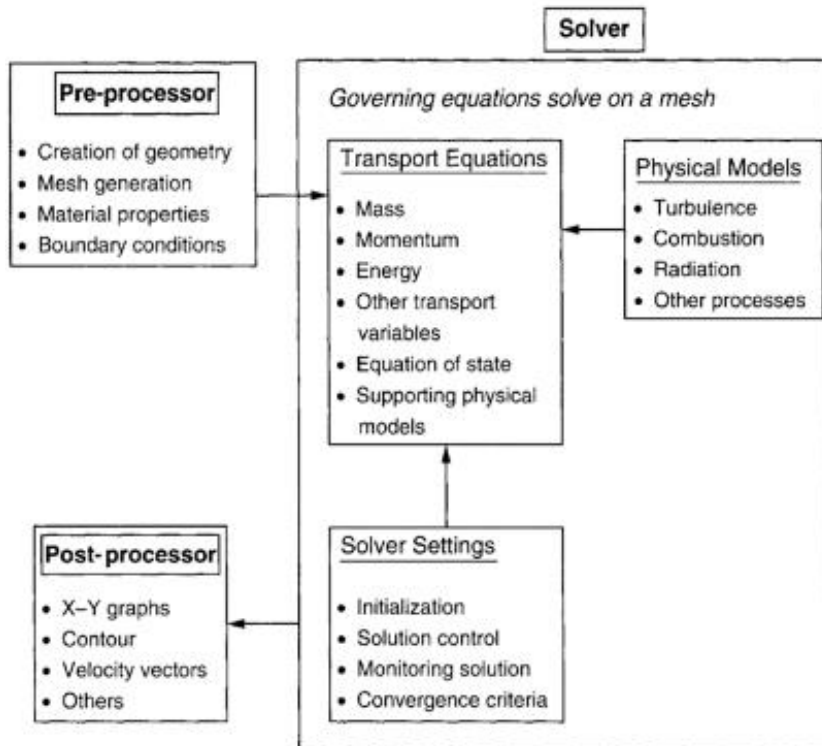


Figure 3.1. Three main phases of CFD [36]

For the current study, the simulation was set concerning Figure 3.1, and the problem was specified in three main stages. First, the simulation domain was modeled with SolidWorks software. Then, the model was meshed with the meshing tool, and the boundary conditions were determined in agreement with the physical model. Finally, the numerical simulation of the flow around the propeller was performed with Fluent. A brief flow chart for the current simulation procedure is shown in Figure 3.2.



Figure 3.2. Simulation procedure

The Multiple Reference Frame model (MRF) approach was applied to analyze the flow around the 16-inch propeller. The 16x4 carbon fiber propeller, shown in Figure

3.3, is a retail outlet product, and it was 3D scanned for use in CFD analysis to obtain accurate results. CFD simulations were conducted in both vertical climb and hovering flight flow conditions at various rotational speeds and free-stream velocities. An interface was used to transfer flow data to the adjacent domain zones. Reynolds-Averaged Navier-Stokes simulations were performed by implementing the  $k-\omega$  turbulence model.



Figure 3.3. 16-inch carbon fiber propeller and 3D scanned 16-inch carbon fiber propeller

CFD simulation matrix is summarized in Table 3.1. Hovering flight performance simulations were conducted at 1050, 2000, and 3150 RPM values for the 16-inch carbon fiber propeller. In order to perform vertical climb flight performance simulations, 16-inch carbon fiber propeller RPM was set to 2000 and 3150, and the flow domain speed was adjusted to 3.42 and 5.42 m/s. Rotor-propeller arm interaction simulations were conducted in hovering flight at 3150 RPM.

Table 3.1. CFD simulation conditions

Propeller Type	Hovering Flight Tests	Vertical Climb Flight Tests	
	Rotational speed of the propeller (RPM)	Rotational speed of the propeller (RPM)	Free Stream Velocity (m/s)
Carbon Fiber 16x4	1050, 2000 and 3150	2000 and 3150	3.42 and 5.42
Carbon Fiber 16x4 with different arms	3150	-	-

### 3.2.2. Flow domain and boundary conditions

Flow domain and boundary conditions are demonstrated in Figure 3.4a, where velocity inlet boundary condition describes the entrance of the flow, and the outflow

boundary condition defines exit of flow. The velocity inlet and outflow boundary conditions can vary according to the flight configuration. The solution domain consists of a rotating domain in which the propeller is surrounded by a cylinder, and a stationary domain. These domains are connected with the interfaces. Only half of the flow domain was computed in the propeller-only simulations as a two-bladed propeller was analyzed, which allows for a rotational periodicity. For the arm structure investigation part, on the other hand, the complete physical domain was simulated. The 16-inch propeller is placed in the center of the rotational domain, as shown in Figure 3.4b.

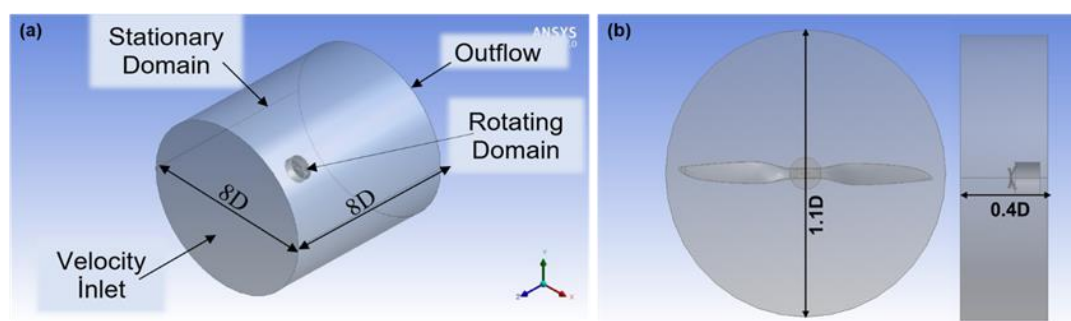


Figure 3.4. (a) Flow domain and boundary conditions, (b) Rotating domain

Height of the stationary domain is eight times the diameter of the propeller. For the rotating domain that is located at the center of the stationary domain, the cylinder enclosure dimensions are adjusted to be  $1.1D$  and  $0.4D$ . The test bench elements, used during the experimental part of the study, were not included in the flow domain. As mentioned in the studies of Sunan [36] and Rajendran [8], the boundaries of the stationary domain were set far enough from the propeller so that the flow was not affected. Stationary and Rotating domains were sized based on numerical studies performed in previous computational campaigns that are explained in section 1.1.3. Stajuda et al. [3] investigated the influence of the different rotating domain thicknesses on the results of thrust and power by using MRF approach. Numerical results of Stajuda et al. were also considered for the current study to prevent recirculation of the flow, which can lead to convergence problems.

Table 3.2. Boundary conditions for the flow domain in hovering flight simulations

No	Boundary	Boundary Condition	Turbulence Boundary Condition
1	Inlet	Static pressure 100kPa	1% Turbulence intensity
2	Outlet	Static pressure 100kPa	1% Turbulence intensity
3	Propeller	No slip in MRF $W=0$	-
4	Motor	No-slip $V=0$	-
5	Strut	No-slip $V=0$	-

Table 3.3. Boundary conditions for the flow domain in vertical climb flight simulations

No	Boundary	Boundary Condition	Turbulence Boundary Condition
1	Inlet	Velocity inlet $V=V_{\text{freestream}}$	1% Turbulence intensity
2	Outlet	Static pressure 100kPa	1% Turbulence intensity
3	Propeller	No-slip in MRF $W=0$	-
4	Motor	No-slip $V=0$	
5	Strut	No-slip $V=0$	

Cell zone condition setup of Fluent was adjusted to the rotational speed value of the 16-inch propeller for rotating domain. The ambient conditions of the 16-inch propeller test were used as simulation inputs. Boundary conditions utilized in CFD simulations are presented in Table 3.2 and Table 3.3 for hovering and vertical climb flight, respectively. Pressure outlets were set atmospheric. The no-slip condition was adjusted on the walls. Due to the rotation of the propeller, the no-slip condition is forced in relative velocity in moving reference frame. Velocity inlet conditions were implemented for both vertical climb and hovering flight configurations. For rotor-propeller arm interaction and hovering flight simulations, the velocity inlet and

outflow boundary conditions were set as pressure outlet. Free-stream velocity values were utilized at the inlet with a turbulence intensity of 1% for vertical climb flight conditions. The turbulence intensity values adjusted based on METUWIND C3 wind tunnel measurements [40]. Solution methods of the simulation setup were achieved by applying Table 3.4 to the analysis.

Table 3.4. Solution Methods

Pressure-Velocity Coupling	
Scheme	SIMPLE (Semi-Implicit Method for Pressure-Linked Equations)
Spatial Discretization	
Gradient	Least Square Cell-Based
Pressure	Second Order
Momentum	Second Order Upwind
Turbulent Kinetic Energy	First Order Upwind
Specific Dissipation Rate	First Order Upwind

### 3.2.2.1. SIMPLE algorithm

SIMPLE algorithm is used for solving incompressible flow equations robustly. It was developed by Patankar [45]. SIMPLE algorithm is a pressure-based solver and utilizes a relationship between velocity and pressure to acquire the pressure field. In order to get the solution of the pressure values, the Poisson's equation is employed (Equation 3.15).

$$\frac{\partial}{\partial x_i} \left( \frac{\partial p}{\partial x_i} \right) = - \frac{\partial}{\partial x_i} \left[ \frac{\partial(\rho u_i u_j)}{\partial x_j} \right] \quad (3.15)$$

The working principle of the SIMPLE solution algorithm is given in Figure 3.5. In the SIMPLE algorithm, the problem is being solved iteratively, and steps are proceeded until the convergence criteria are fulfilled.

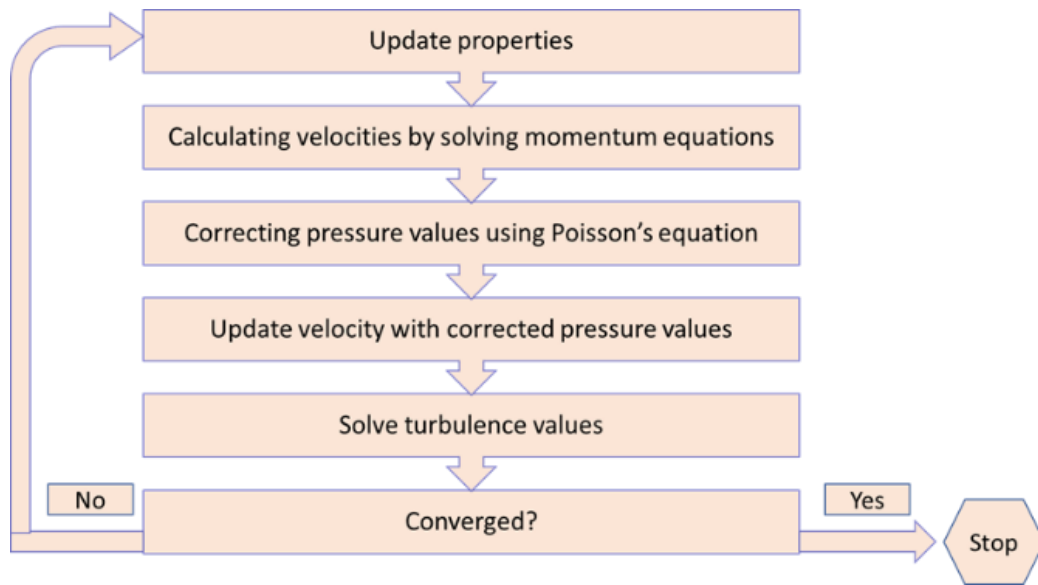


Figure 3.5. Overview of the SIMPLE solution algorithm working principle

### 3.2.3. Mesh generation

The flow domain is divided into small subdomains called mesh or grid cells to investigate the properties of the fluid flow. The required flow properties are defined by the solution of RANS equations for each cell iteratively. The mesh for the study was generated using the mesh generation tool in Ansys Fluent 17.0. The solution mesh is crucial because it supplies a specific depiction of the geometry of interest. A high-quality computational grid is essential to provide reliable results and to solve the boundary layer on the propeller surface properly. The mesh quality prominently affects the rate of convergence, simulation time and performance. Typically, grids fall into two categories, structured and unstructured grids. Generally, simple computational domains are meshed with the structured mesh cells, while complex shaped control volumes are meshed with the unstructured mesh cells. Structural grids mostly consist of hexahedral cells, while unstructured grids mostly consist of pyramid, tetrahedral, hexahedral, polyhedral, or wedge cells (or hybrid of these) in 3D. The mesh used for the current study is unstructured and composed of tetrahedral elements in both domains. Meshes were generated based on the numerical studies performed in the previous computational campaigns that are explained in section 1.1.3.

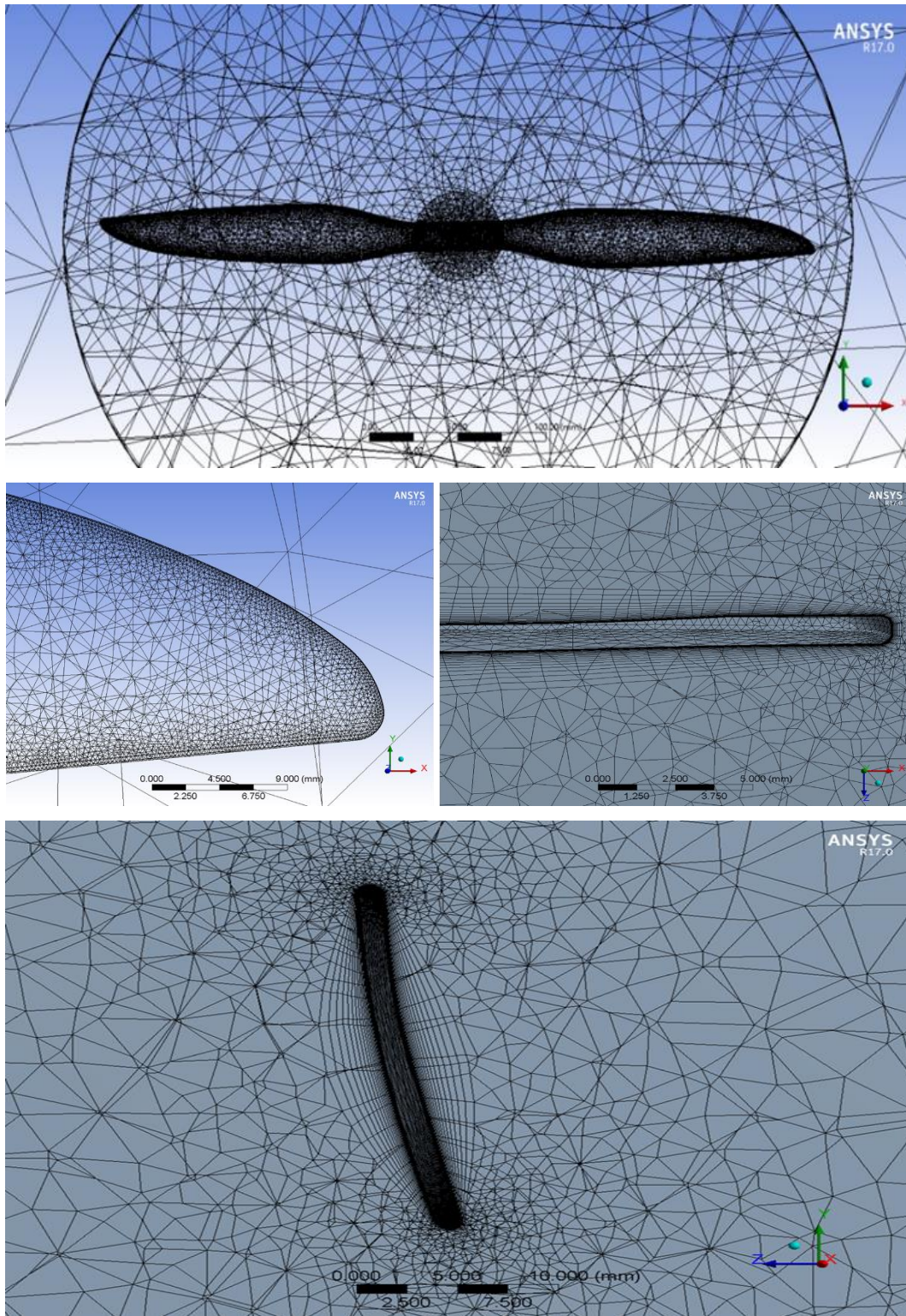


Figure 3.6. A portion of the mesh with respect to the propeller blade surface, propeller blade tip, and 0.75% blade span position

A portion of the mesh with respect to the propeller blade surface, propeller blade tip, and 0.75% blade span position is shown in Figure 3.6. While cell sizes are small near the propeller wall, they increase in size as the distance increases. For the rotating domain, where the meticulous approach was necessary, the cells were generated to be in a smaller size along with the propeller and motor. Body sizing was applied for rotating domain. Inflation was inserted to the arm structure, propeller, and motor region. The same meshing method was applied both to the single propeller, and the arm structure. While adapting a complex physical phenomenon to a CFD simulation, unstructured meshing requires minimum user intervention compared to the structural meshing. The mesh sizing parameters used in the current study are tabulated in Table 3.5. Further details about the mesh sizing will be represented in mesh independency part of this chapter.

Table 3.5. Mesh Sizing Parameters

Size Function	Proximity and Curvature
Relevance Center	Fine
Initial Size Seed	Active Assembly
Smoothing	High
Transition	Slow
Span Angle Center	Fine
Curvature Normal Angle	34°
Num Cells Across Gap	Default
Proximity Size Function Sources	Faces and Edges
Min Size	0.400 mm
Proximity Min Size	0.822 mm
Max Face Size	82.200 mm
Max Tet Size	164.420 mm
Growth Rate	1.210
Automatic Mesh-Based Defeaturing	On
Defeaturing Tolerance	0.200 mm
Minimum Edge Length	1.252e-003 mm

### 3.3. Rotor Frame-arm Interaction Study

After validating the numerical simulations with the thrust and torque measurement results of the 16-inch propeller, four different arm shapes were included in the numerical flow solutions for the 16-inch propeller in order to assess their influence on the aerodynamic rotor performance (Figure 3.7). These are Eppler Arm, 25mm cylindrical tube, 25mm square tube, and 25mm square tube with a 10mm slot.

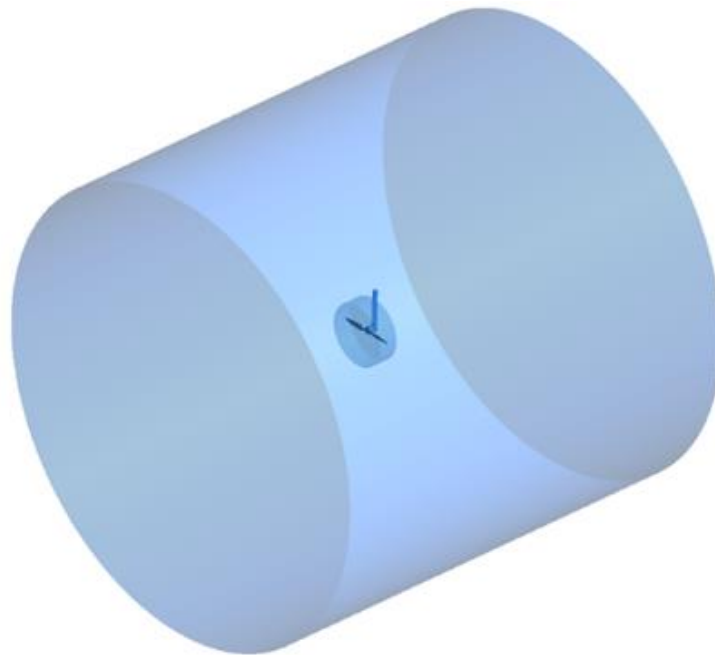


Figure 3.7. Isometric view of flow domain including arm structure with 16-inch propeller

Eppler Arm is the arm with E 862 Airfoil, which was designed especially for non-lifting struts by Richard Eppler [46]. The airfoil shown in Figure 3.8 was used to design arm for the 16-inch propeller. The airfoil is scaled to have a maximum thickness of 25 mm.

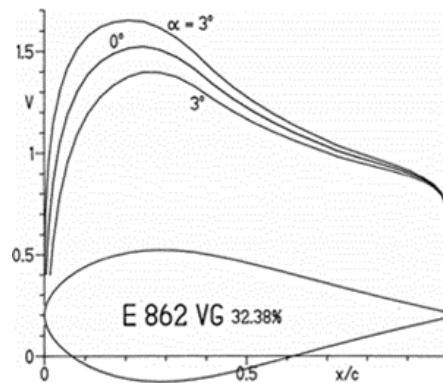


Figure 3.8. E 862 strut airfoil [46]

In the last step, torque and thrust values from the four cases in hovering flight were compared with each other. This comparison will be presented in Chapter 4. The schematics of arm propeller configurations are shown in Figure 3.9.

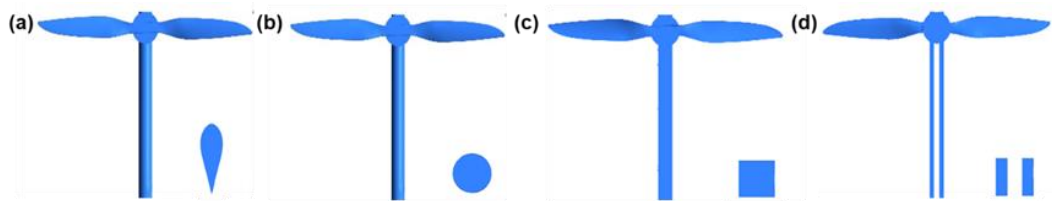


Figure 3.9. (a) Eppler Arm, (b) Cylinder Arm, (c) Square Arm, (d) Slotted Square Arm

### 3.3.1. MRF model approach

In this study, the MRF approach was chosen because of the computing time advantage. MRF model is a steady-state approach in which separate cell regions can be appointed with distinct rotational and translational speeds [47]. The MRF model is, perhaps, the most straightforward approach for multiple zones and commonly used rotary machinery design and propeller studies. MRF model is used for interaction investigations between the stationary and rotating regions of the computational domain. In order to obtain the solution of the unsteady problem, MRF model provides a rotation effect to the rotating regions by utilizing the steady calculations [34]. Flow data is transferred to the adjacent domain zones with an interface. The MRF model

approach was scientifically approved for propeller simulations and provided reliable results (shown in section 1.1.3).

For the current study, rotational speed of the 16-inch propeller was set using the MRF approach. In the MRF approach, the mesh of the rotating domain does not move, and the propeller itself does not rotate relative to the surrounding domain. This means that the rotating domain does not actually rotate. Moreover, the velocity resulting from the rotation of domain is transferred to the convenient nodes numerically.

For the arm structure study, six new rotating domains were created to check the consistency of the MRF approach in itself. In order to achieve this, the propeller was rotated six times with 30-degree intervals (Figure 3.10). CFD simulation results of these analyses will be shown in section 4.2.1).

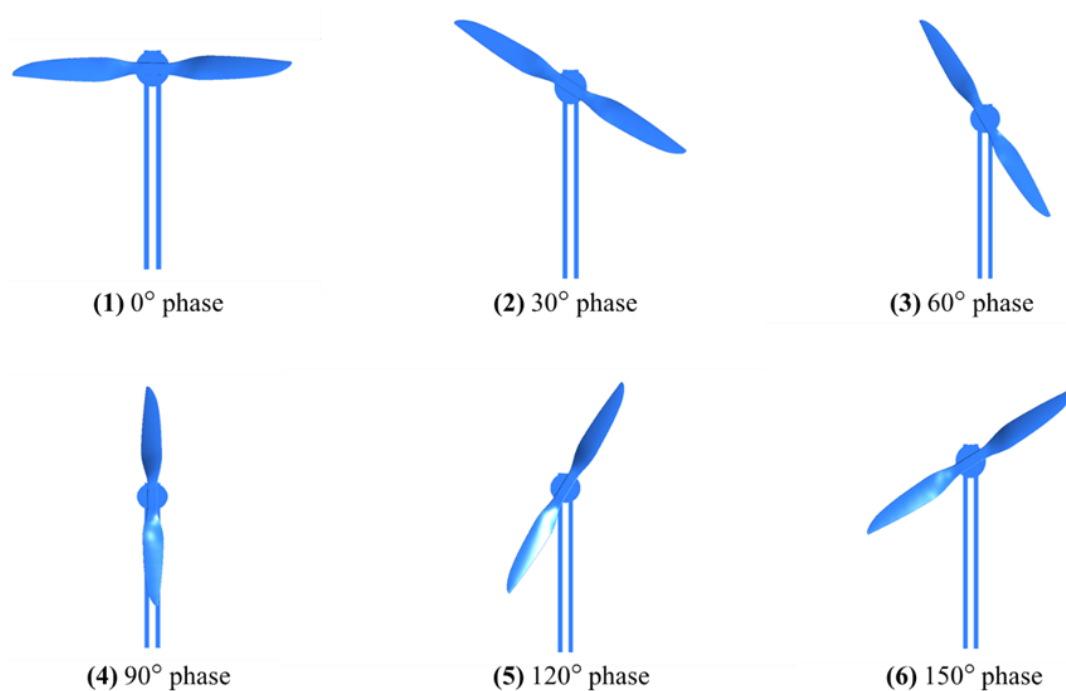


Figure 3.10. Six different phases used for the arm interaction study

### 3.4. Numerical Method Verification and Validation

#### 3.4.1. Mesh and iteration number independency analysis

Mesh generation is one of the most critical parts of CFD simulations. In simulation studies, if the results of the analysis are not affected by the number of nodes, it is independent of the mesh structure. When performing numerical analysis, simulation results must be independent of the number of mesh cells. Within the scope of the mesh independency study, performance results of the hovering and vertical climb flight configurations of the propeller-only case, which can vary depending on the density of the number of mesh cells, are discussed. All other simulation properties were kept constant. The results of the different analysis were compared with each other and the corresponding experimental data. Seven different grids were created by changing the meshing parameters for hovering and vertical climb flight configurations. The amount of mesh cells generated for these simulations is presented in Table 3.6.

Table 3.6. Number of Mesh Cells

Hovering/Vertical Climb Flight
3,026,139
2,388,233
1,888,208 (Fine)
1,295,716
732,857 (Medium)
526,541
477,644 (Coarse)

Mesh independency study simulations were performed by implementing standard  $k-\omega$  turbulence model at 2000 rpm for both flight configurations. For the vertical climb flight simulations, free stream velocity was set to 3.42 m/s. Examples of coarse, medium, and fine mesh generated on the propeller surface are presented in Figure 3.11a, Figure 3.11b, and Figure 3.11c, respectively. Only half of the flow domain was

meshed in propeller-only simulations. Therefore, the full domain propeller study would consist of at least twice the number of mesh cells.

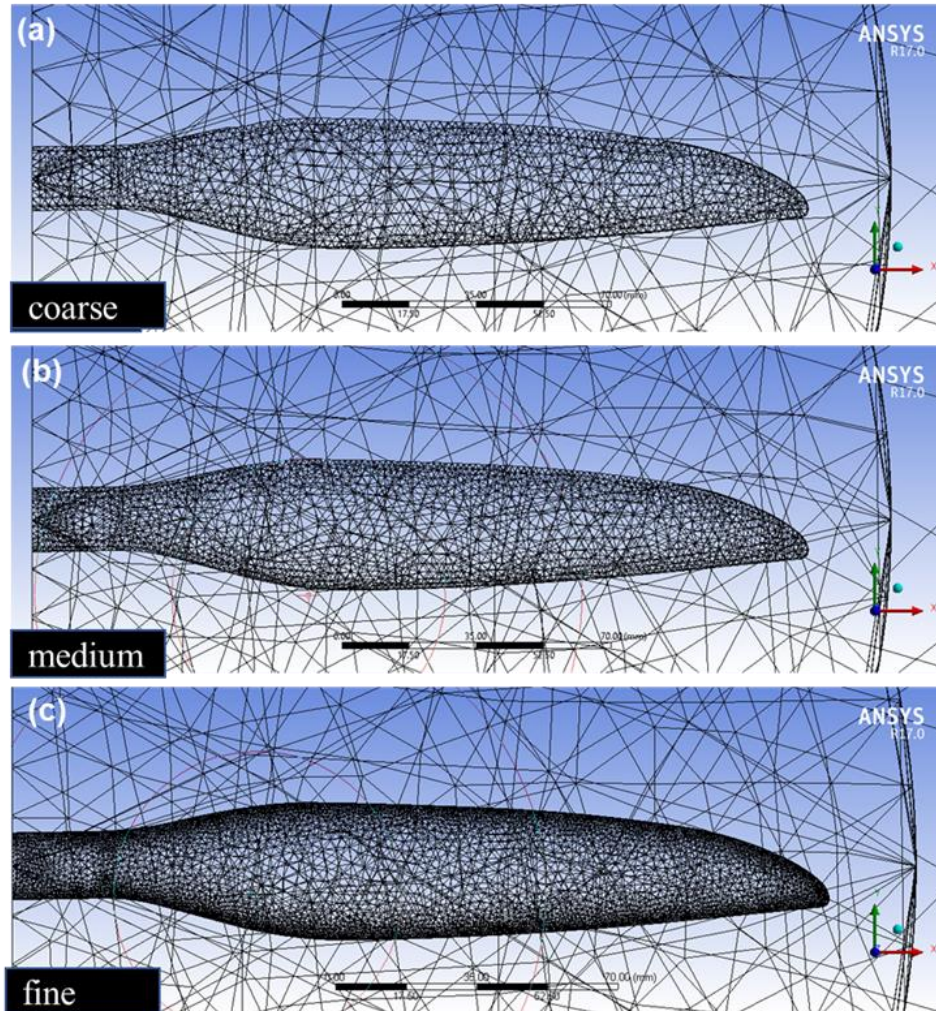


Figure 3.11. Examples of coarse, medium, and fine mesh generated on the propeller surface  
(a) coarse surface mesh, (b) medium surface mesh, (c) fine surface mesh

The solution time and accuracy of the analysis are the factors that determine the selection of the appropriate meshing for the current study. Although the analysis time for the model with a large number of cells seems quite high, the results for the models with different cell numbers do not present significant differences. No dependence on the number of mesh cells was observed as long as the number of cells was over 1.5 million. In order to save time, performance analyzes of the current study were

performed with a model with approximately 1.5 million cells. Because, besides the memory and processor capacity of the solution computer, the time taken for the solution plays a critical role for many points in numerical studies. Mesh independency study for hovering and vertical climb flight configurations are shown in Figure 3.12 and Figure 3.13, respectively. Thrust and torque values, versus the corresponding mesh cell numbers are shown in figures. Mesh independency study was carried out at 2000 rpm for both flight configurations. For vertical climb flight, free stream velocity was set to 3.42 m/s.

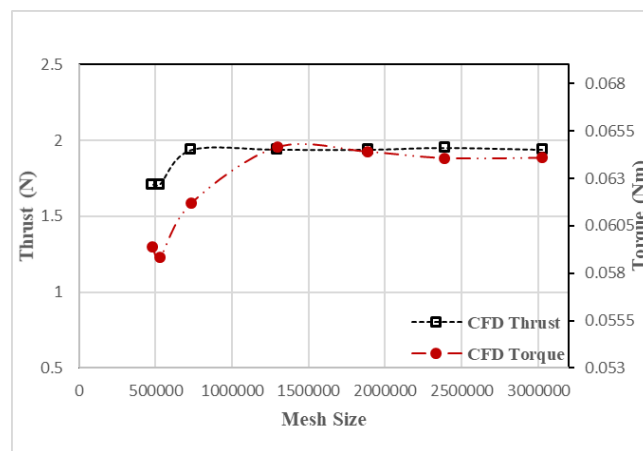


Figure 3.12. Mesh independency study results for hovering flight at 2000 rpm

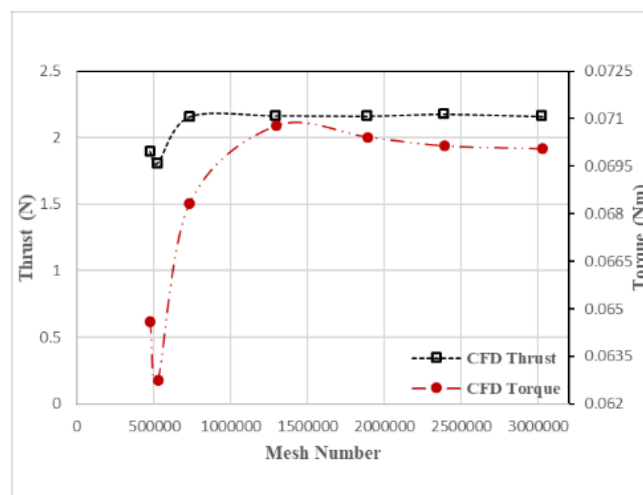


Figure 3.13. Mesh independency study results for vertical climb flight at 2000 rpm

In addition to the comparison of thrust and torque results,  $y^+$  values were also checked as part of the mesh independency study.

In order to solve the propeller performance simulation with high precision, the mesh was formed denser around the propeller, the motor, and the strut arm. In order to perform accurate analysis in this region, the cell structure was formed such that  $y^+$  was below less than one. In Figure 3.14  $y^+$  contour of the propeller with the cylinder arm is presented for 90° phase, and in there the maximum  $y^+$  is 0.627. This value indicates that the  $y^+$  requirement is met to achieve accurate results.

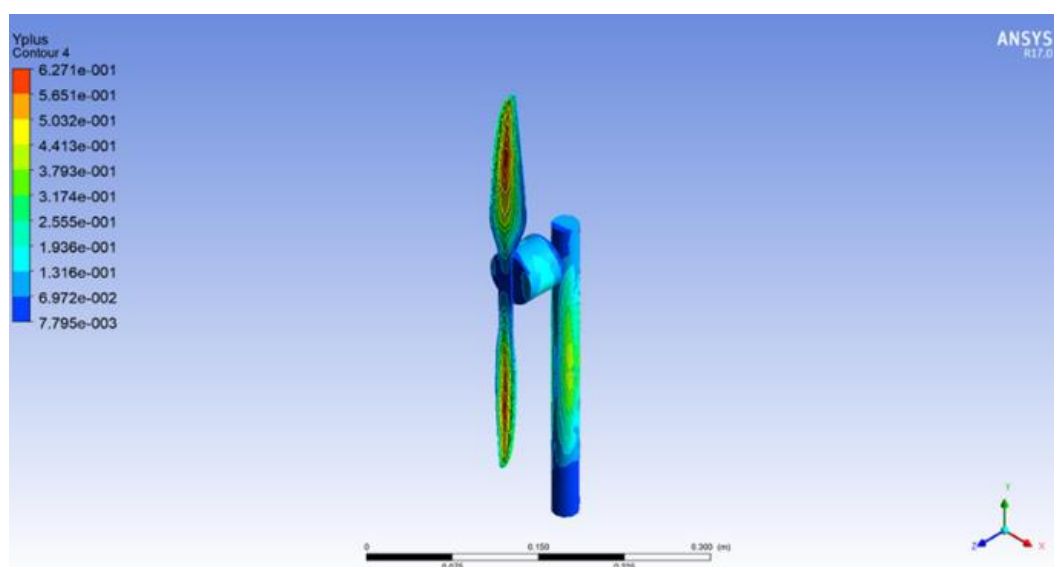


Figure 3.14.  $y^+$  contour of the propeller with cylinder arm

In the current CFD simulation study, continuity equation, momentum equations, turbulent kinetic energy, and dissipation equations are solved iteratively, and the magnitudes of differences are explained with residuals. For a CFD simulation, the solution should not be changed according to the number of iterations. Therefore, an iteration independence analysis was carried out for the propeller performance simulations.

Each computation step in a CFD algorithm can be tracked by monitoring convergence. A converged solution is acquired by a good quality mesh with accurate control

settings. In this simulation study, it was seen that propeller performance solutions ensured the convergence tolerance. Residuals for 2000 rpm vertical climb flight simulation is given in Figure 3.15 in which it is seen that the residuals remain stable in an appropriate magnitude after 1750 iterations.

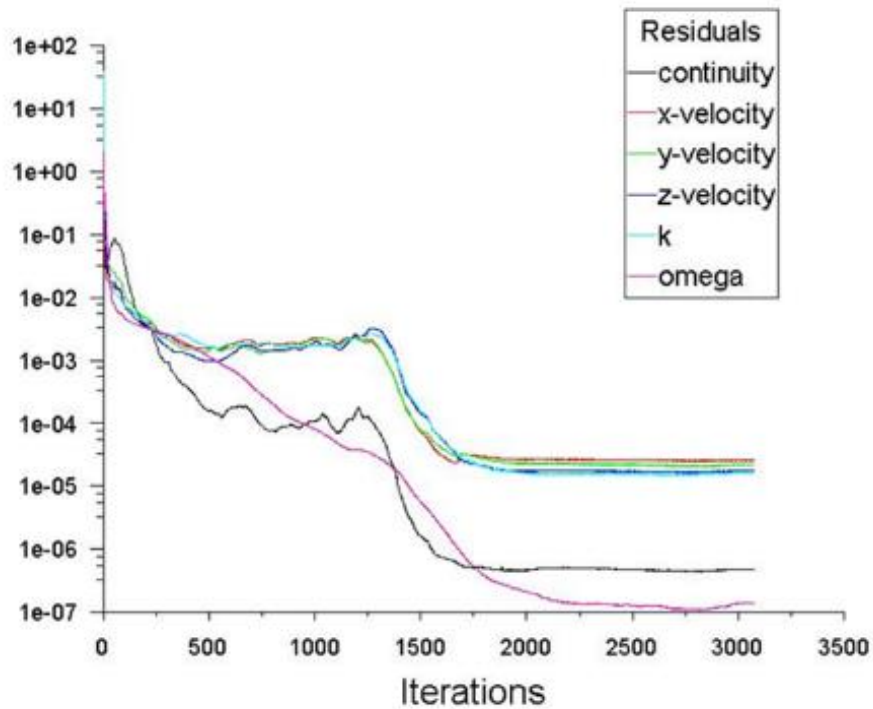


Figure 3.15. Residuals for 2000 rpm vertical climb flight simulation

### 3.4.2. Model independency analysis

There is no multi-purpose turbulence model that will apply to all working conditions and solve problems correctly. For this reason, many turbulence models are considered. For each flow condition, there is a more appropriate turbulence model that better reflects the situation. Therefore, the turbulence models which are valid for the propeller flow analysis and offer the closest values compared to the test results were investigated.

In addition to mesh independency study, six different turbulence models were investigated to evaluate the optimal model to estimate propeller performance. The

standard  $k-\epsilon$ , Spalart Allmaras (SA), standard  $k-\omega$ , transition  $kkl\omega$ ,  $k-\omega$  SST, transition SST turbulence models were evaluated for both hovering and vertical climb flight configurations. Detailed theoretical knowledge of these models can be found in the "ANSYS Fluent Theory Guide" document [47]. The flow domain with the number of 2 million mesh cells was preferred for the model independency study. For hovering flight, the comparison of the thrust and torque simulation results between the turbulence models are given in Figure 3.16 and Figure 3.17, respectively. Model independency study was performed at 2000 rpm for both flight configurations.

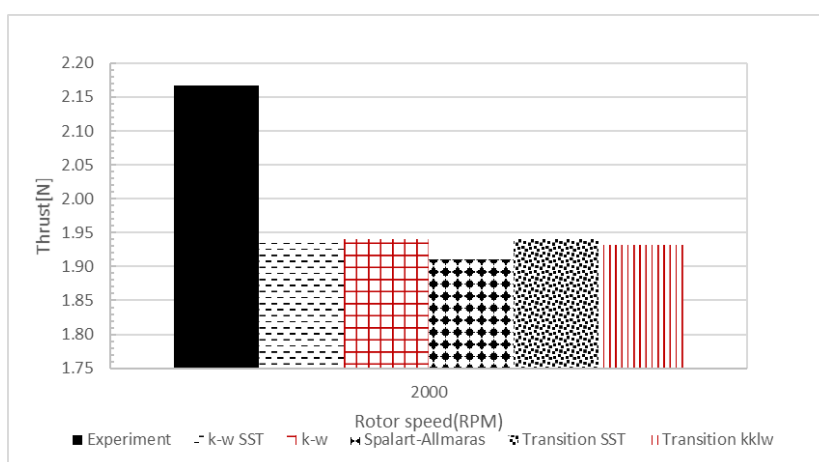


Figure 3.16. Thrust value comparison between the measurement data and different turbulence models at 2000rpm for hovering flight

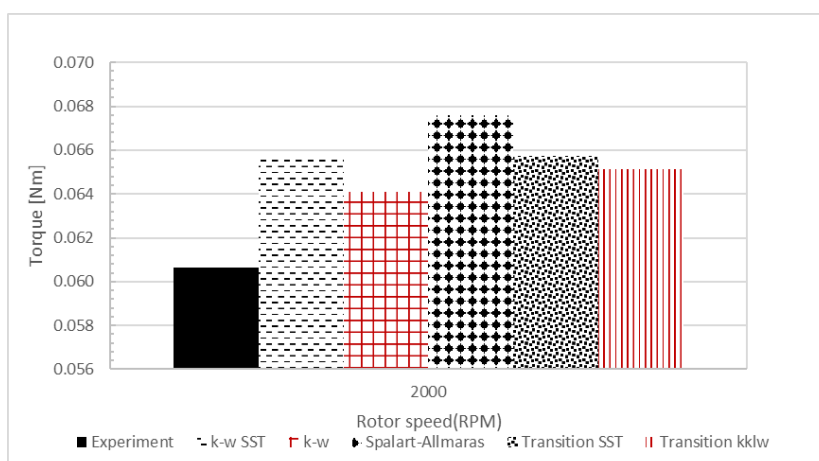


Figure 3.17. Torque value comparison between measurement data and different turbulence models at 2000rpm for hovering flight

For the vertical climb flight, free stream velocity was adjusted to 3.42 m/s, and the comparison of the thrust and torque simulation results between the turbulence models are shown in Figure 3.18 and Figure 3.19, respectively. Although a similar trend was observed with all of the considered turbulence models, the  $k-\omega$  turbulence model yielded the most accurate results, so it was selected to be used in the subsequent numerical solutions.

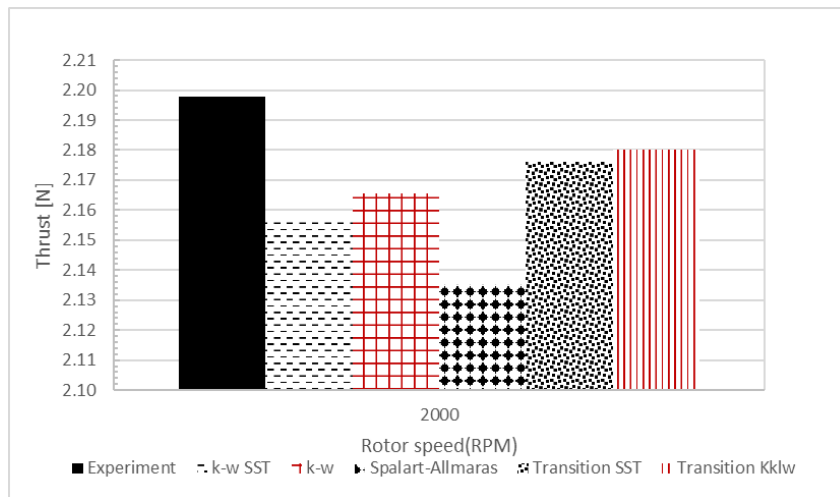


Figure 3.18. Thrust value comparison between measurement data and different turbulence models at 2000rpm for vertical climb flight

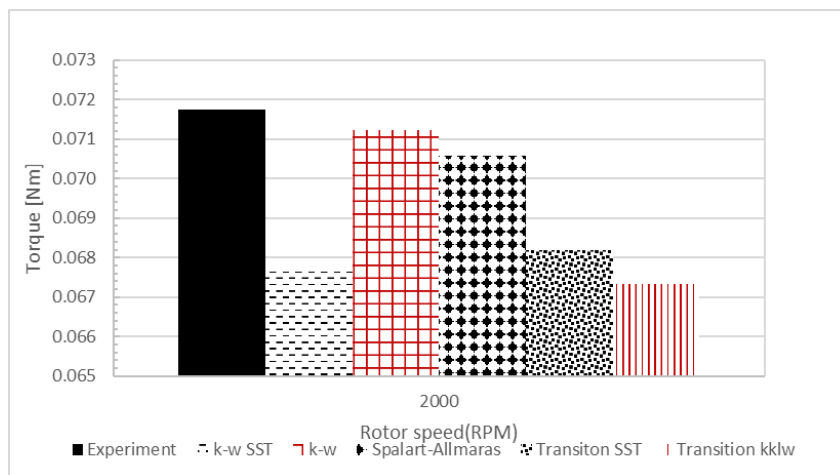


Figure 3.19. Torque value comparison between measurement data and different turbulence models at 2000rpm for vertical climb flight



## CHAPTER 4

### RESULTS AND DISCUSSION

In this chapter, the 16-inch carbon propeller test and CFD results will be presented and discussed. First, thrust and torque measurement results will be compared with the numerical simulations performed in ANSYS Fluent. The thrust and torque data will be plotted to interpret the aerodynamic performance of the propeller at different flight configurations. In the second section, the interaction between propellers and rotor frame arm of different geometries and the influence of the frame arm distance to the propeller on the aerodynamic performance of the rotor in hovering flight will be described.

#### 4.1. Carbon Fiber 16x4 Propeller Test and CFD Results

##### 4.1.1. Hovering flight results

Figure 4.1 and Figure 4.2 show the comparisons of the Carbon Fiber 16x4 propeller hovering flight performance results obtained from CFD simulations and tests. Hovering flight thrust and torque values versus the corresponding RPMs are shown in figures.

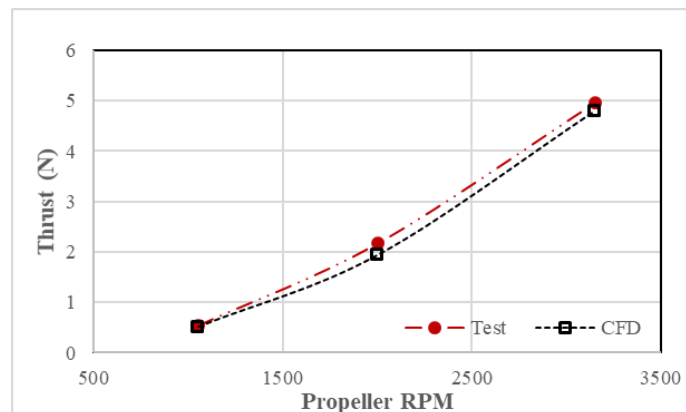


Figure 4.1. Comparison of the thrust values obtained from CFD simulations and measurements for the Carbon Fiber 16x4 propeller in hovering flight

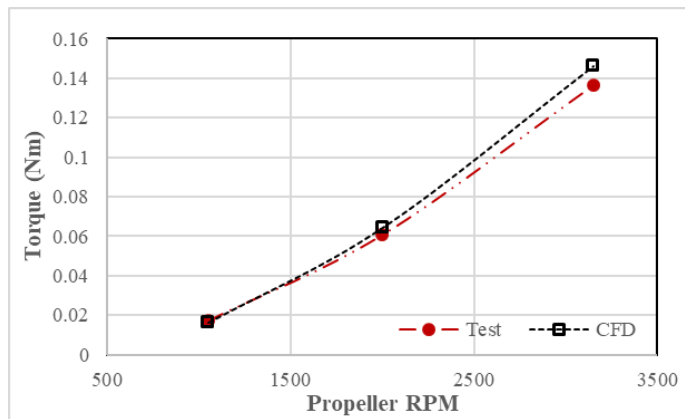


Figure 4.2. Comparison of the torque values obtained from CFD simulations and measurements for the Carbon Fiber 16x4 propeller in hovering flight

Hovering flight CFD simulation and test results comparison data presented in Figure 4.1 and Figure 4.2 are shown in Table 4.1. The values of the thrust and power coefficient are given in the table, and the difference between them is demonstrated as a percentage. As a result of the hovering flight CFD simulation comparison study, when compared with the relevant test data, a maximum discrepancy of 10.44% for the thrust coefficient and 7.28% for the power coefficient is obtained. The average disparity value achieved from the test results comparison data is 5.79% for the thrust coefficient and 6.19% for the power coefficient. Investigation proved that the applied CFD method displays a good agreement with the tests of the current study.

Table 4.1. Thrust and Power coefficient comparison data for hovering flight

Carbon Fiber 16x4 Propeller						
	CFD		Test		Comparison	
RPM	$C_T$	$C_P$	$C_T$	$C_P$	$C_T$ Difference	$C_P$ Difference
1050	0.0542	0.0264	0.0564	0.0278	-3.91%	-5.09%
2000	0.0561	0.0288	0.0627	0.0271	-10.44%	6.21%
3150	0.0559	0.0263	0.0577	0.0246	-3.02%	7.28%

### 4.1.2. Vertical climb flight results

Vertical climb flight CFD simulation and test results comparison are given in Figure 4.3 and Figure 4.4. Thrust and power coefficients versus the corresponding advance ratio values are shown in figures for vertical climb flight.

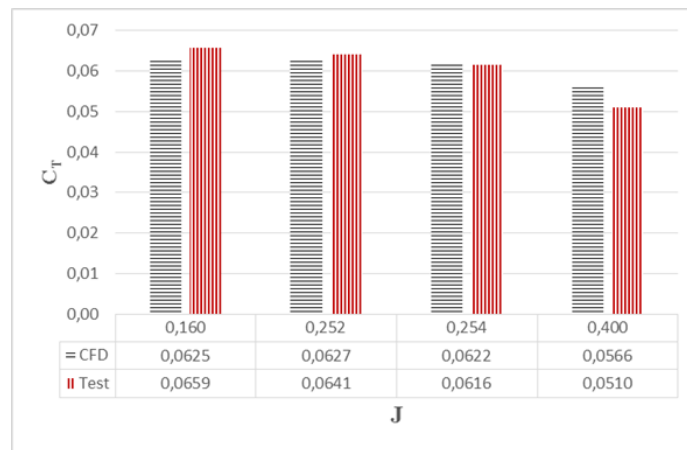


Figure 4.3. Comparison of the thrust coefficient obtained from CFD simulations and measurements for the Carbon Fiber 16x4 propeller in vertical climb flight

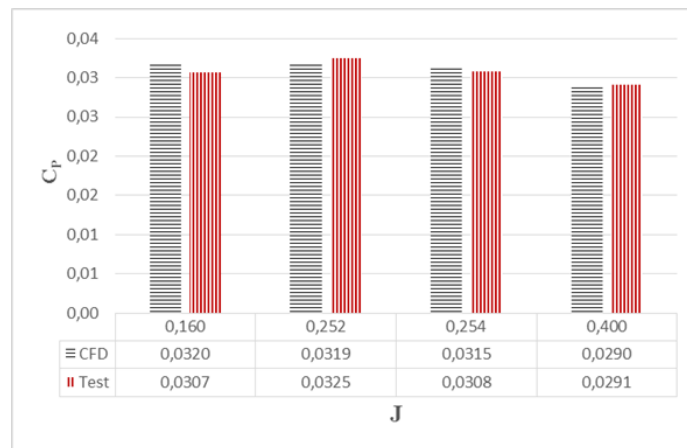


Figure 4.4. Comparison of the power coefficient obtained from CFD simulations and measurements for the Carbon Fiber 16x4 propeller in vertical climb flight

Vertical climb flight CFD and test results comparison data introduced in Figure 4.3 and Figure 4.4 are shown in Table 4. The values of the thrust and power coefficient are represented in the table, and the difference between them is indicated as a

percentage. As a result of the vertical climb flight CFD simulation comparison study, a maximum inconsistency of 10.81% for the thrust coefficient and 4.06% for the power coefficient is obtained when compared with the relevant test data. The average difference value achieved from the test results comparison data is 4.78% for the thrust coefficient and 2.18 % for the power coefficient. Thus, the comparative analysis has proven that the CFD methodology, which is based on the use of MRF technique, can be considered to be a reliable approach for the simulation of the flow in a similar setup.

Table 4.2. Thrust and Power coefficient comparison data for vertical climb flight

Carbon Fiber 16x4 Propeller								
			CFD		Test		Comparison	
RPM	J	V	C <sub>T</sub>	C <sub>P</sub>	C <sub>T</sub>	C <sub>P</sub>	C <sub>T</sub> Differ.	C <sub>P</sub> Differ.
2000	0.160	3.42	0.0625	0.0320	0.0659	0.0307	-5.14%	4.06%
3150	0.252	3.42	0.0627	0.0319	0.0641	0.0325	-2.26%	-2.05%
2000	0.254	5.42	0.0622	0.0315	0.0616	0.0308	0.90%	2.38%
3150	0.400	5.42	0.0566	0.0290	0.0510	0.0291	10.81%	-0.24%

Since some differences were observed in comparison of the test results for APC Slow Flyer 11x4.7 propeller between METU and UIUC tests, the majority amount of differences in the comparison of the CFD and the test results of carbon fiber 16x4 propeller can be considered due to some errors in the experimental measurements.

#### 4.2. Rotor Frame-arm Interaction Study Results

In this section, prominent pressure contours of the rotor frame-arm of four different geometries will be examined to investigate the main features of the flow field. The rotor frame-arm simulations were considered for hovering flight configuration. The contours are shown at the center plane (y-z plane) of the arm. In the second part of this section, the effects of the distance of the rotor frame-arm to the propeller will be

evaluated. The interaction study was conducted with three different rotor frame-arm distance (i.e., small, middle, and long-distance). In section 4.2.1, consistency of the MRF approach in itself for rotor-propeller arm interaction study will be examined. In Section 4.2.2, the pressure contours of the small distance square-frame arm configuration will be explored to examine whether the presence of the arm has any effect on performance. In section 4.2.3, small distance frame-arm configuration performance comparison between the four different frame-arm will be explained. In section 4.2.4, pressure contours of the small, middle, and long-distance frame-arm configurations will be evaluated for the Eppler frame-arm and the slotted square frame-arm, respectively.

The comparison of the results and their analysis is not a simple subject for the model with frame-arm. Therefore, these contours maintain a good chance to visualize the changes on the pressure distributions for the frame-arm simulations. These simulations were anticipated to provide as a general case to define the aerodynamics occurring on the rotor frame-arm flow field.

#### **4.2.1. Examining the consistency of MRF approach in itself**

Theoretical information about the MRF model approach is given in section 3.3.1. In this section, the MRF approach analysis results of the propellers positioned at different angles (propeller was rotated six times within the simulation domain with 30-degree intervals) will be examined. In Figure 4.5, the comparison of the thrust coefficients with and without the presence of the rotor-frame arm shapes are shown with respect to the different propeller phase angles. According to the results, although the propeller position is different, similar trends are observed for the 12 propeller positions.

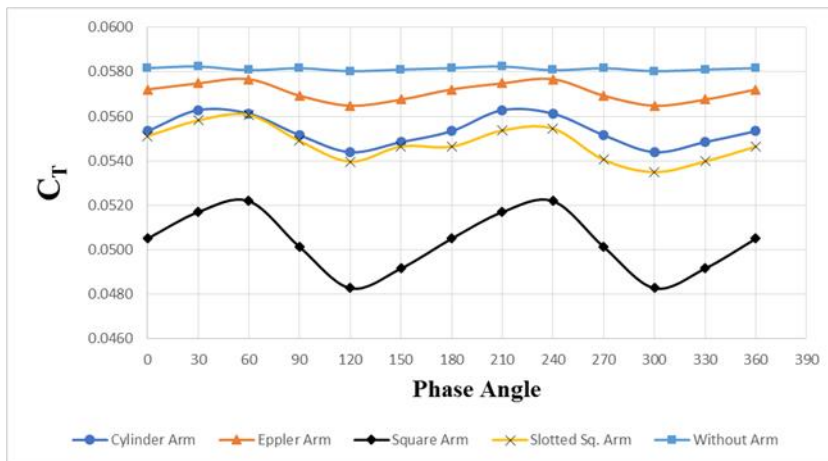


Figure 4.5. Comparison of the thrust coefficients obtained from CFD simulations for the different arm shapes with respect to the different propeller phase angles

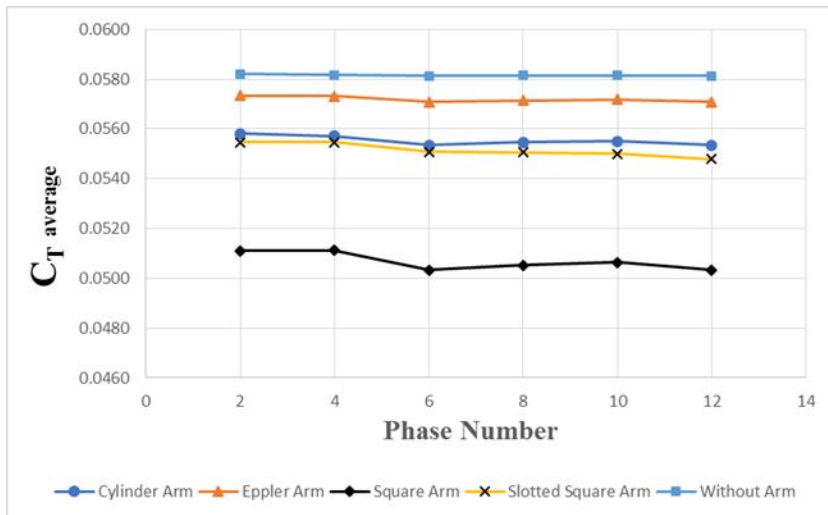


Figure 4.6. Comparison of the thrust coefficient averages for the different arm shapes with respect to the different propeller phase numbers

The thrust coefficient results which are obtained from the different propeller phases (see Figure 4.5) are averaged to examine the phase number effect. Figure 4.6 presents the comparison of the averaged thrust coefficients versus the phase number for with and without the presence of the rotor-frame arm shapes. As shown in the figure, the average thrust coefficient results are approximately the same as the number of phase increases. The simulation results in different phase angles have yielded similar results

for all arm types. As a result of this study, it can be said that the angle that the rotor is positioned has no significant effect on the simulation results carried out with the MRF approach.

#### 4.2.2. Performance comparison with and without the presence of the arm

In Figure 4.7 and Figure 4.8, the pressure contours for two different rotor phases ( $0^\circ$  and  $90^\circ$  degrees of rotation) with and without the presence of the small distance square arm with respect to the center of the arm are depicted.

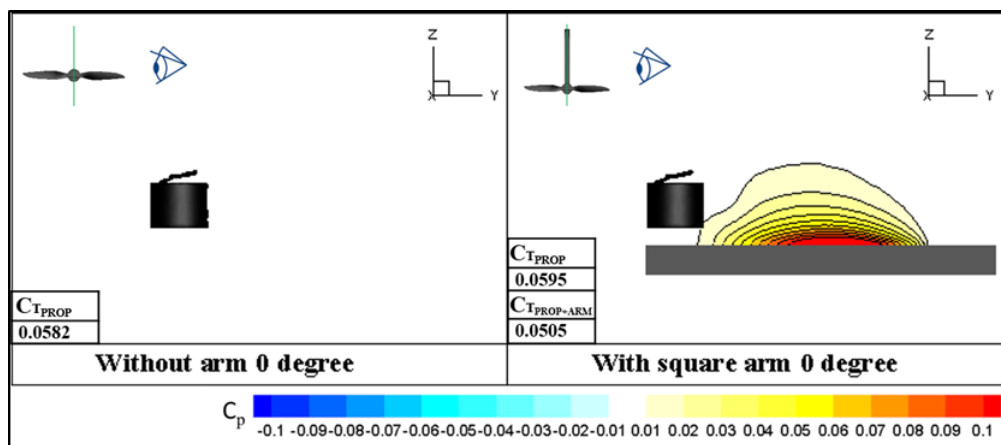


Figure 4.7. Pressure contours with and without the presence of the small distance square arm with respect to the center of the arm at the  $0^\circ$  rotor phase

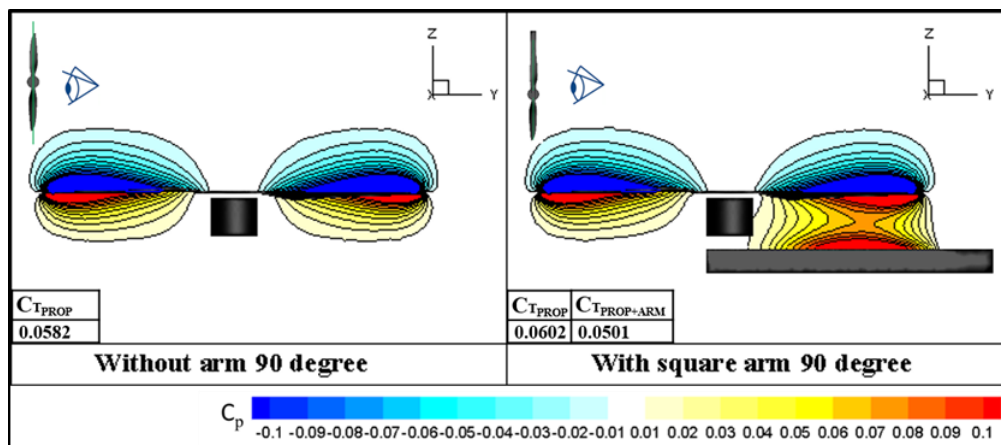


Figure 4.8. Pressure contours with and without the presence of the small distance square arm with respect to the center of the arm at the  $90^\circ$  rotor phase

There is a high-pressure zone when the arm is present compared to the without arm case in all phases which results in negative thrust in the downward direction leading to a decrease in the total rotor-arm thrust. However, this high-pressure zone increases the thrust generated by the propeller. The interaction between the rotor and the rotor affects the aerodynamic performance of the propeller in a way analogous to ground effect.

### 4.2.3. Effect of the different rotor frame arm shapes

In order to have a proper configuration to achieve a lower negative arm thrust following a greater total thrust, four different arm shapes are investigated. For this purpose, cylindrical, square, slotted square and Eppler arm are considered. Small distance rotor frame-arm configuration performance comparison between the four different rotor frame-arm will be described in this section.

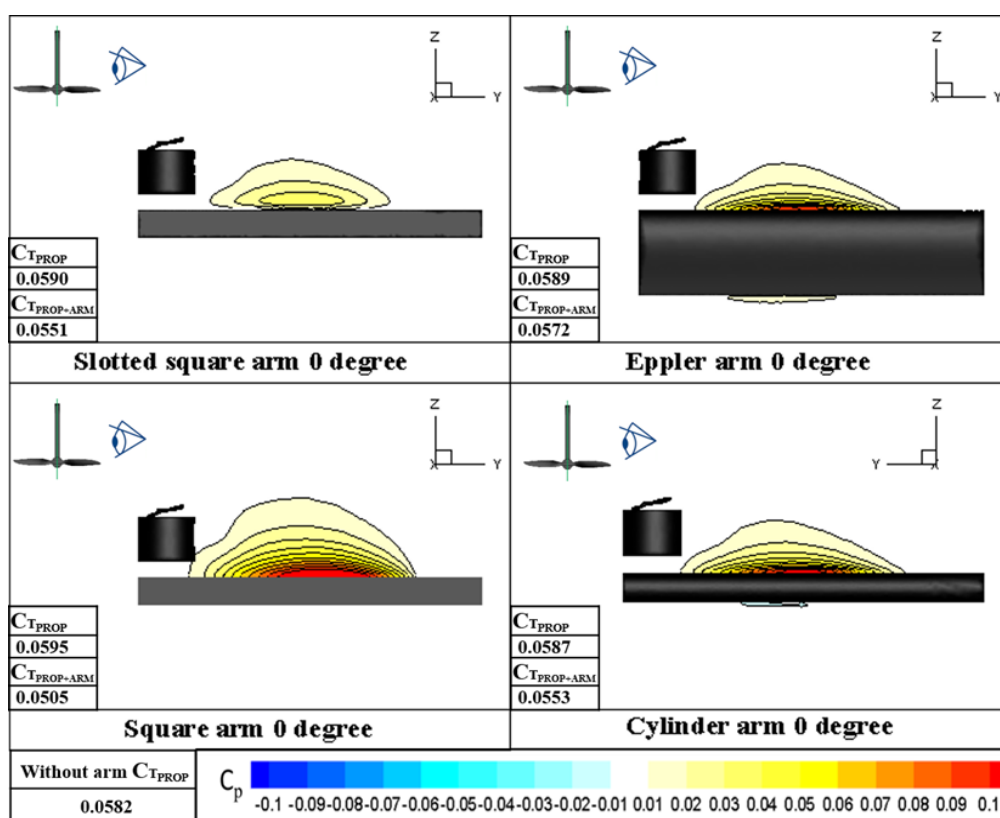


Figure 4.9. Pressure contours of the four different arms with respect to the center of the arm at the 0° rotor phase

The middle and long-distance rotor frame-arm configuration performance comparison will be defined in section 4.2.4. In Figure 4.9, the pressure contours with the presence of square, slotted square, Eppler and cylindrical arm are shown with respect to the center of the arm at the  $0^\circ$  rotor phase. In all cases, there is a high-pressure zone when the arm is available producing a downward negative arm thrust. This follows with a decrease in total rotor-arm thrust compared to the without arm case.

This positive pressure region is stronger in the case of the square arm, which also yields a higher propeller thrust due to increased pressure level at the pressure side of the propeller. However, this increased positive pressure region also increases the negative thrust (viz. drag) of the propeller arm and as a result, a small total thrust coefficient is obtained (see Table 4.3). In accordance with the aforementioned statement regarding the analogous ground effect, the decrease in the solidity of the propeller arm (i.e. slotted arm geometry) results in a decrease in the thrust coefficient of the propeller. However, arm-generated-drag also decreases and as a result a higher total thrust coefficient than the square arm geometry is achieved with the slotted arm. This is also justified by the contours of velocity magnitude in the wake of the arm, as shown in Figure 4.10. Velocity deficit is the highest in the case of the square arm, whereas the Eppler geometry yields the minimum deficit compared to the other cases, which manifests itself in the numbers tabulated in Table 4.3.

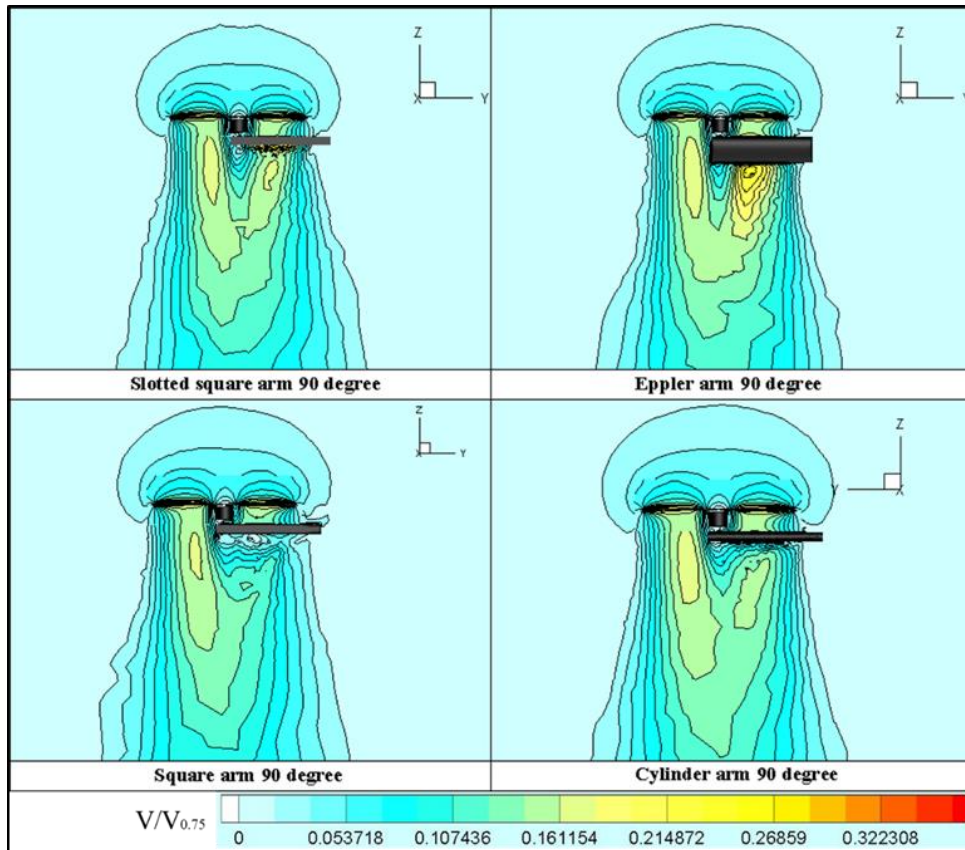


Figure 4.10. Velocity contours at the 90° rotor phase for different arm shapes

In hovering flight condition, the efficiency of the propeller  $\eta_{prop}$  is calculated using momentum theory as defined by Theys [38]. The efficiency of the propeller  $\eta_{prop}$  is described by Equations (4.1) - (4.5).

In these equations,  $T$  (N) is the thrust produced by propeller,  $Q$  (Nm) is torque,  $\omega$  (rad/s) is the angular speed of the propeller,  $A$  (m<sup>2</sup>) is the disk area of the propeller,  $\rho$  (kg/m<sup>3</sup>) is the density of the fluid,  $V_0$  is the airspeed ahead of the propeller,  $V_i$  is the airspeed at the propeller disk and  $v_i$  is the induced velocity. The propeller efficiency ( $\eta_{prop}$ ) is identified as the ratio between the induced power ( $P_i$ ) and the required mechanical power ( $P_{mech}$ ).

In these equations,  $T$  (N) is the thrust produced by propeller,  $Q$  (Nm) is torque,  $\omega$  (rad/s) is the angular speed of the propeller,  $A$  (m<sup>2</sup>) is the disk area of the propeller,  $\rho$

( $\text{kg/m}^3$ ) is the density of the fluid,  $V_0$  is the airspeed ahead of the propeller,  $V_1$  is the airspeed at the propeller disk and  $v_i$  is the induced velocity. The propeller efficiency ( $\eta_{prop}$ ) is identified as the ratio between the induced power ( $P_i$ ) and the required mechanical power ( $P_{mech}$ ).

$$V_0 = 0 \quad (4.1)$$

$$V_1 = v_i \quad (4.2)$$

$$T = 2\rho A(v_i)^2 \quad (4.3)$$

$$P_i = TV_1 \quad (4.4)$$

$$\eta_{prop} = \frac{P_i}{P_{mech}} = \frac{T^{\frac{3}{2}}}{Q\omega\sqrt{2\rho A}} \quad (4.5)$$

Small distance rotor frame-arm configuration performance analysis shows that by adding an arm to the simulation domain, the thrust of the propeller will be decreased. Among the different arm shapes, Eppler arm has the highest thrust coefficient value and total efficiency. Thus, the Eppler arm is the optimum arm shape among these four different arms. The average thrust coefficient, power coefficient, and efficiency values for different arm shapes are shown in Table 4.3. In the table,  $C_{Tprop}$  stands for the thrust coefficient generated by the propeller only, whereas  $C_{Tprop+arm}$  and  $C_{Pprop+arm}$  are the total thrust and power coefficient of the propeller-arm structure, respectively.

Table 4.3. Average Efficiency, Thrust and Power coefficient values of different rotor arm shapes

	Without Arm	Cylinder Arm	Eppler Arm	Square Arm	Slotted Sq. Arm
$C_{Tprop}$	0.05813	0.05880	0.05878	0.05960	0.05891
$\eta_{prop}$	0.38659	0.39020	0.39049	0.39597	0.39306
$C_{Tprop+arm}$		0.05535	0.05710	0.05034	0.05508
$C_{Pprop+arm}$	0.02893	0.02916	0.02912	0.02932	0.02903
$\eta_{prop+arm}$		0.35641	0.37384	0.30745	0.35542

The results of this study expose that the propeller-Eppler arm configuration has 4.89%, 21.59%, and 5.18% greater propeller efficiency than that of the propeller-cylindrical arm, propeller-square arm, and propeller-slotted square arm configurations, respectively. For average total thrust values in all four different arms, the Eppler arm produces the minimum negative thrust following with the highest total thrust compared to three other cases. On the other hand, the thrust coefficient generated by the propeller only case ( $C_{Tprop}$ ), the square arm geometry scores the best.

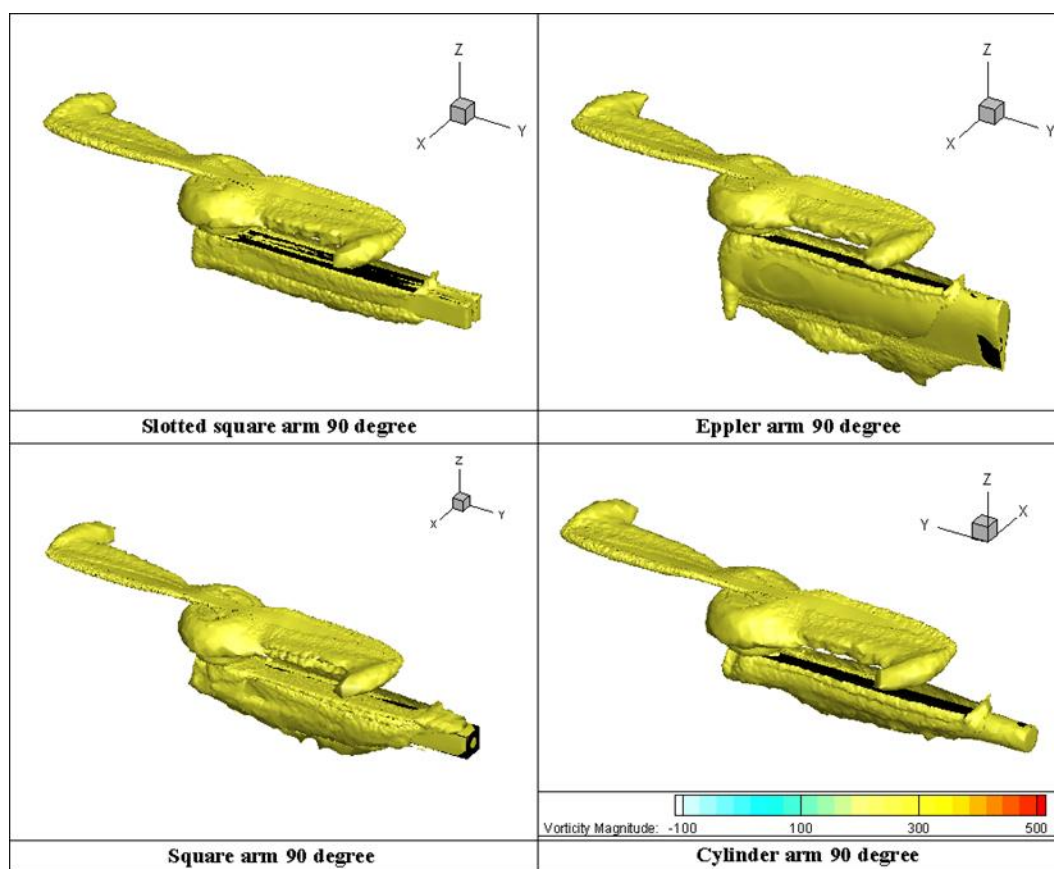


Figure 4.11. 3D vorticity magnitude representation of flow for the different arms

In figure 4.11, 3D vorticity magnitude representation of flow for the four different arm shapes is given. Iso-surface is drawn at the specified value of 300 for the 3D vorticity magnitude representation of the flow.

#### 4.2.4. Rotor frame arm distance effects

For small distance rotor frame-arm configuration, the Eppler arm was shown to have the best performance among four different cases. In order to analyze the effect of rotor frame-arm distance on the rotor performance, two more cases for Eppler and slotted square arm configurations are considered at which in the middle-distance case, the distance between the rotor and arm is considered as 35 mm (20 mm shifted from the initial case), and in the long-distance case, the distance between the rotor and arm is considered as 55 mm (40 mm shifted from the initial case). The sketch of the initial (short) distance case is depicted in Figure 4.12.

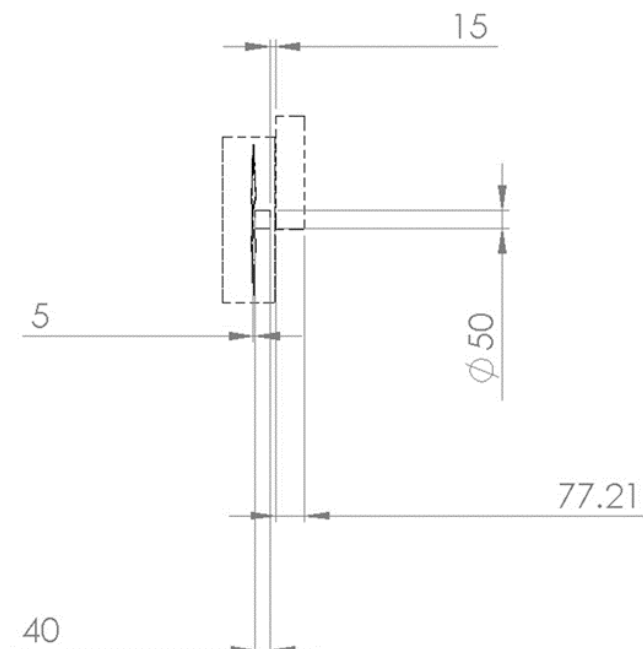


Figure 4.12. A sketch of small rotor frame-arm distance configuration in mm

Pressure contours of the small, middle, and long-distance rotor frame-arm configurations for Eppler and slotted rotor frame-arms are depicted in Figure 4.13. Although the presence of solid surfaces increases the thrust generation of the propeller, the negative thrust caused by the high-pressure region above the arm decreases the

overall thrust of the arm structure. As seen in Figure 4.13, this interaction effect decreases with increasing arm distance.

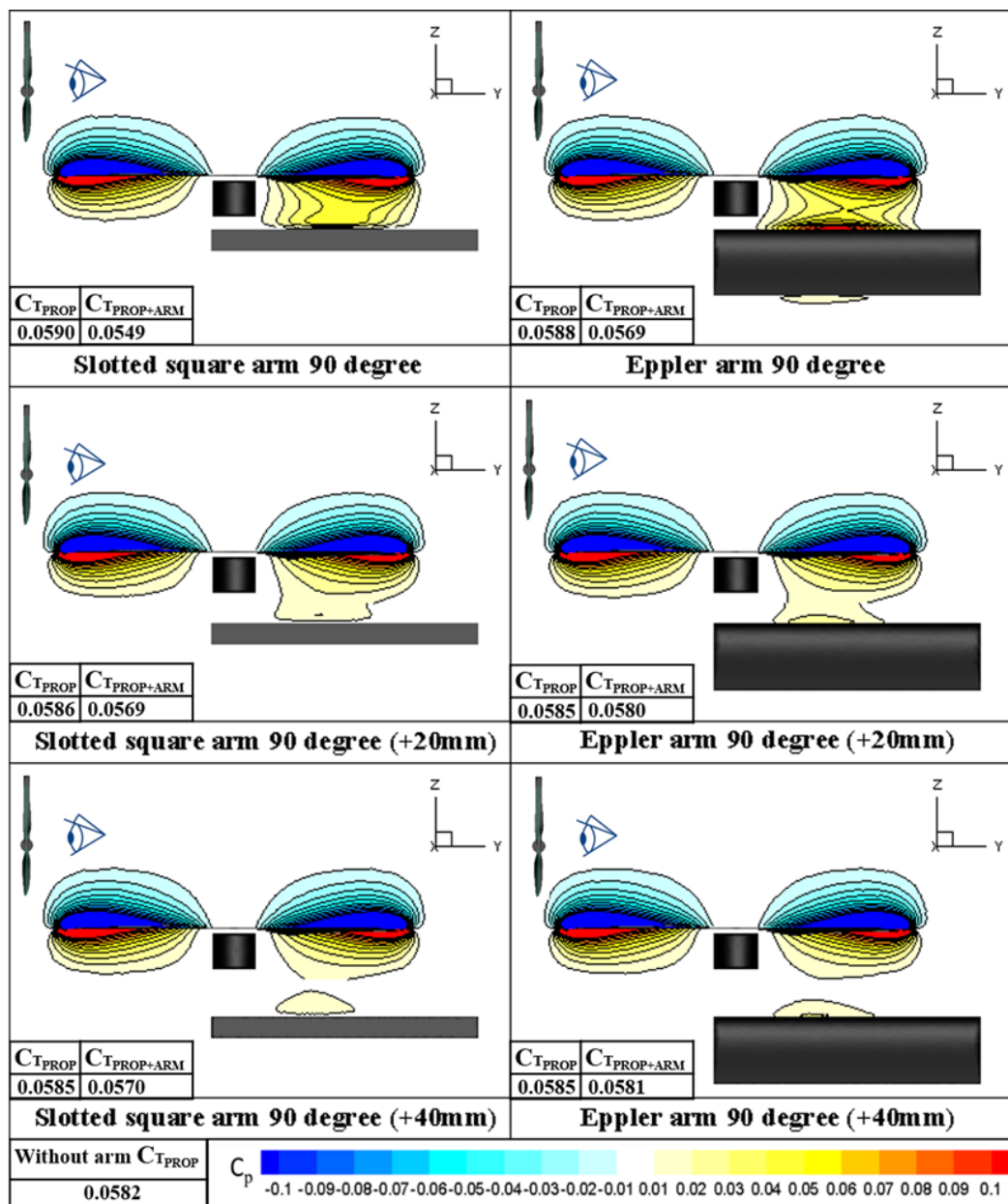


Figure 4.13. The pressure contour of the slotted square and Eppler arm with respect to the center of the arm for the small rotor frame-arm distance

The average thrust coefficient and efficiency values for Eppler and Slotted square arm shown in Table 4.4. In the table,  $C_{Tprop}$  stands for the thrust coefficient generated by the propeller only, whereas  $C_{Tprop+arm}$  is the total thrust coefficient of the propeller-arm structure.

Table 4.4. Average Efficiency, Thrust and Power coefficient values of Eppler and Slotted square arm at the different rotor arm distances

Arm Type	$C_{Tprop}$	$\eta_{prop}$	$C_{Tprop+arm}$	$C_{Pprop+arm}$	$\eta_{prop+arm}$
Eppler Arm	0.05878	0.39049	0.05710	0.02912	0.37384
Eppler Arm (+20mm)	0.05851	0.38935	0.05807	0.02901	0.38497
Eppler Arm (+40mm)	0.05844	0.38897	0.05806	0.02898	0.38517
Slotted Sq Arm	0.05891	0.39306	0.05508	0.02903	0.35542
Slotted Sq. Arm (+20mm)	0.05856	0.39001	0.05702	0.02899	0.37475
Slotted Sq. Arm (+40mm)	0.05847	0.38924	0.05710	0.02898	0.37562

Averaged  $C_{Tprop+arm}$  and  $\eta_{prop+arm}$  results show that middle and long-distance Eppler arm geometries are more efficient than the small-distance Eppler and slotted square arm shapes. On the other hand, the average thrust coefficient formed by the middle and long-distance arms scores similarly. This situation shows that, after the middle-distance arm distance, the negative thrust in downward direction leading to a decrease in total rotor-arm thrust diminishes.



## CHAPTER 5

### CONCLUSION

This study numerically investigates the interaction between rotor and rotor frame-arm of different geometries in hovering flight by utilizing the commercially available computational fluid dynamics (CFD) solver software ANSYS Inc. Fluent 17. Therefore, four different rotor frame-arm configurations, (i.e., Eppler Arm, 25mm cylindrical tube, 25mm square tube, and 25mm square tube with a 10mm slot) are generated and investigated.

Two different propellers, APC Slow Flyer 11x4.7 propeller, and 16x4 carbon fiber propeller were used in this study. The thrust and torque measurements captured by using a loadcell with these propellers in the test section of the low-speed METUWIND C3 wind tunnel at the Rüzgem (Metuwind). In order to validate the experimental setup of used in this study, the APC Slow Flyer 11x4.7 propeller was utilized for propeller measurements comparison between the current data and measurements taken by Brandt [6]. The computational study phase of this study was carried out by using the 3D scanned version of a 16x4 carbon fiber propeller. Reynolds-Averaged Navier-Stokes simulations were performed by implementing the  $k-\omega$  turbulence model. The numerical simulations were validated for hovering and vertical climb flight conditions with the thrust and torque measurement results of the 16x4 carbon fiber propeller at the various rotational speeds. Hovering flight performance simulations were conducted at 1050, 2000, and 3150 rpm values. Vertical climb flight performance simulations were performed at 2000 and 3150 rpm values by adjusting the flow domain speed to 3.42 and 5.42 m/s. Rotational speeds of the 16-inch propeller were set using the MRF approach.

As a result of the hovering flight CFD comparison study, when compared with the relevant test data, a maximum discrepancy of 10.44% for thrust and 7.28% for torque

were obtained. For vertical climb flight, a maximum disparity of 10.81% for the thrust coefficient and 4.06% for the power coefficient was obtained. These results have proven that the applied CFD method is reliable for other similar CFD studies.

After validating numerical simulations, four different arm geometries added to the validated CFD model to assess their effect on the aerodynamic performance of the rotors. Arm structure study simulations were conducted using the MRF approach at 3150 rpm and hovering flight conditions. It was found that all arm geometries have a negative effect on the aerodynamic performance when compared to the without arm configuration. This negative effect is prominent, especially for the 25mm square tube arm. Overall, the Eppler arm geometry configuration gives the best performance at hovering flight.

The results of this study showed that the propeller-Eppler arm configuration has 4.89%, 21.59%, and 5.18% greater propeller efficiency than that of the propeller-cylindrical arm, propeller-square arm, and propeller-slotted square arm configurations, respectively.

In all cases, the presence of solid surfaces increases the thrust generation of the propeller, the negative thrust caused by the high-pressure region above the arm decreases the overall thrust of the arm structure. This positive pressure region is stronger in the case of the square arm, which also yields a higher propeller thrust due to increased pressure level at the pressure side of the propeller.

For future works, the following suggestions can be considered:

- The study can be progressed by performing full-body quadrotor experiments and CFD simulations at different flight conditions.
- CFD simulations can be repeated by utilizing the sliding mesh models to analyze the transient flow.
- A wider range of propellers can be investigated, and with the learning of this research, an efficient new propeller can be designed.

- In order to decrease the energy consumption of a quadrotor, it would be interesting to perform experiments and CFD simulations by changing some other design parameters. Some of the listed parameters can be investigated for this purpose.
  - Distance between the rotors
  - Rotors with/without a shroud
  - Coaxial and overlapping rotors
- Wind turbines, marine propeller performance and design studies can be performed with the information on experimental and numerical methodology obtained from the present study.



## REFERENCES

- [1] D. Erdos and S. E. Watkins, "UAV autopilot integration and testing," *2008 IEEE Region 5 Conference*. 2008.
- [2] N. Jodeh, P. Blue, and A. Waldron, "Development of Small Unmanned Aerial Vehicle Research Platform: Modeling and Simulating with Flight Test Validation." 2012.
- [3] N. Haala, M. Cramer, F. Weimer, and M. Trittler, "Performance Test on Uav-Based Photogrammetric Data Collection," *ISPRS - International Archives of the Photogrammetry, Remote Sensing and Spatial Information Sciences*, vol. XXXVIII-1/. pp. 7–12, 2012.
- [4] M. Percin, *Aerodynamic Mechanisms of Flapping Flight*. 2015.
- [5] G. Hoffmann, H. Huang, S. Waslander, and C. Tomlin, "Quadrotor Helicopter Flight Dynamics and Control: Theory and Experiment," no. August, pp. 1–20, 2012.
- [6] "The Pioneers : An Anthology : Louis Charles Bréguet (1880 - 1955)," 1907. [Online]. Available: <http://www.ctie.monash.edu.au/hargrave/breguet.html>.
- [7] R. W. Deters, G. K. Ananda, and M. S. Selig, "Reynolds Number Effects on the Performance of Small-Scale Propellers," in *32nd AIAA Applied Aerodynamics Conference*, 2014, no. June, pp. 1–43.
- [8] H. Kutty and P. Rajendran, "3D CFD Simulation and Experimental Validation of Small APC Slow Flyer Propeller Blade," *Aerospace*, vol. 4, no. 1. p. 10, 2017.
- [9] M. Bağçe, "Design and Performance Evaluations of the Propeller of a UAV," 2015.
- [10] D. Gamble and A. Arena, "Automated Dynamic Propeller Testing at Low Reynolds Numbers." 2014.
- [11] P. B. S. Lissaman, "Low-Reynolds-Number-Airfoils." pp. 223–239, 1983.
- [12] J. B. Brandt and M. S. Selig, "Propeller Performance Data at Low Reynolds Numbers," *49th AIAA Aerospace Sciences Meeting*, no. January. pp. 1–18, 2011.
- [13] B. Pamuk, "Pervane Modellenmesi/Propeller Modelling," Ondokuz Mayıs University, 2012.
- [14] E. Başaran, "Pervane Performansının Analitik ve Sayısal Yöntemlerle

Hesabi/Computational and Analytical Calculation of Propeller Performance,” TOBB Ekonomi ve Teknoloji Üniversitesi, 2017.

- [15] J. B. Brandt, “Small-Scale Propeller Performance At Low Speeds.” 2005.
- [16] Merchant Monal Pankaj, “Propeller performance measurement for low Reynolds number unmanned aerial vehicle applications,” Wichita State University, 2004.
- [17] I. P. Tracy, “Propeller design and analysis for a small, autonomous UAV,” Massachusetts Institute of Technology, 2011.
- [18] B. T. Bettinger, “Manufacturing, Analysis, and Experimental Testing of Multi-bladed Propellers for SUAS,” Oklahoma State University, 2012.
- [19] J. Baranski, M. Fernelius, J. Hoke, C. Wilson, and P. Litke, “Characterization of Propeller Performance and Engine Mission Matching for Small Remotely Piloted Aircraft,” in *47th AIAA/ASME/SAE/ASEE Joint Propulsion Conference & Exhibit*, 2011.
- [20] B. Moffitt, T. Bradley, D. Parekh, and D. Mavris, “Validation of Vortex Propeller Theory for UAV Design with Uncertainty Analysis,” in *46th AIAA Aerospace Sciences Meeting and Exhibit*, 2008, pp. 399–401.
- [21] M. Stajuda, M. Karczewski, D. Obidowski, and J. Krzysztof, “Development of a CFD Model for Propeller simulation,” *Mech. Mech. Eng.*, vol. 20, no. 4, pp. 579–593, 2016.
- [22] D. D. Kaya, “Modeling and Experimental Identification of Quadrotor Aerodynamics,” 2014.
- [23] H. Demirtaş, “Düşük Hızlı Uçaklarda Aerodinamik Pervane Tasarımı ve Optimizasyonu/Aerodynamic Design and Optimization of a Propeller for a Low Speed Aircraft,” Erciyes University, 2006.
- [24] M. Ol, C. Zeune, and M. Logan, “Analytical/Experimental Comparison for Small Electric Unmanned Air Vehicle Propellers,” in *26th AIAA Applied Aerodynamics Conference*, 2008.
- [25] S. Ramakrishna, V. Ramakrishna, A. Ramakrishna, and K. Ramji, “CFD Analysis of a Propeller Flow and Cavitation,” *Int. J. Comput. Appl.*, vol. 55, no. 16, pp. 26–33, Oct. 2012.
- [26] F. Salvatore, C. Testa, S. Ianniello, and F. J. A. Pereira, “Theoretical Modelling of Unsteady Cavitation and Induced Noise,” in *Sixth International Symposium on Cavitation*, 2006.
- [27] M. Morgut and E. Nobile, “Influence of grid type and turbulence model on the numerical prediction of the flow around marine propellers working in uniform inflow,” *Ocean Engineering*, vol. 42, pp. 26–34, 2012.

- [28] X. Wang and K. Walters, “Computational Analysis of Marine-Propeller Performance Using Transition-Sensitive Turbulence Modeling,” *J. Fluids Eng.*, vol. 134, no. 7, p. 071107, 2012.
- [29] E. Benini, “Significance of blade element theory in performance prediction of marine propellers,” *Ocean Engineering*, vol. 31, no. 8–9, pp. 957–974, 2004.
- [30] J. H. Seo, D. M. Seol, J. H. Lee, and S. H. Rhee, “Flexible CFD meshing strategy for prediction of ship resistance and propulsion performance,” *Int. J. Nav. Archit. Ocean Eng.*, vol. 2, no. 3, pp. 139–145, Sep. 2010.
- [31] F. W. Hong and S. T. Dong, “Numerical analysis for circulation distribution of propeller blade,” *Journal of Hydrodynamics*, vol. 22, no. 4, pp. 488–493, 2010.
- [32] W. Tian, B. Song, J. VanZwieten, and P. Pyakurel, “Computational Fluid Dynamics Prediction of a Modified Savonius Wind Turbine with Novel Blade Shapes,” *Energies*, vol. 8, no. 8, pp. 7915–7929, Jul. 2015.
- [33] L. Lu, G. Pan, and P. K. Sahoo, “CFD prediction and simulation of a pumpjet propulsor,” *International Journal of Naval Architecture and Ocean Engineering*, vol. 8, no. 1, pp. 110–116, 2016.
- [34] H. A. Kutty, P. Rajendran, and A. Mule, “Performance analysis of small scale UAV propeller with slotted design,” *2017 2nd International Conference for Convergence in Technology, I2CT 2017*, vol. 2017-Janua, pp. 695–700, 2017.
- [35] G. Chen, B. Chen, P. Li, P. Bai, and C. Ji, “Numerical Simulation Study on Propeller Slipstream Interference of High Altitude Long Endurance Unmanned Air Vehicle,” *Procedia Eng.*, vol. 99, pp. 361–367, 2015.
- [36] B. Sunan, “Computational fluid dynamics analysis of a quadrotor,” Bahçeşehir University, 2014.
- [37] N. D. S. Fernandes, “Design and construction of a multi-rotor with various degrees of freedom,” Technical Univ. of Lisboa, 2011.
- [38] B. Theys, G. Dimitriadis, P. Hendrick, and J. De Schutter, “Influence of propeller configuration on propulsion system efficiency of multi-rotor Unmanned Aerial Vehicles,” no. June, 2016.
- [39] I. Penkov and D. Aleksandrov, “Analysis and study of the influence of the geometrical parameters of mini unmanned quad-rotor helicopters to optimise energy saving,” *International Journal of Automotive and Mechanical Engineering*, vol. 14, no. 4, pp. 4730–4746, 2017.
- [40] “Experimental Aerodynamics Laboratory | RÜZGEM (METUWIND) - Center for wind energy research.” [Online]. Available: <https://ruzgem.metu.edu.tr/en/experimental-aerodynamics-laboratory>. [Accessed: 30-Apr-2019].
- [41] “Model 471B: Thermo-Anemometer Test Instrument - Dwyer Instruments.”

- [Online]. Available: <https://www.dwyer-inst.com/Product/TestEquipment/Thermo-Anemometers/Model471B#specs>. [Accessed: 02-Jun-2019].
- [42] “SD700: Barometric Pressure/Humidity/Temperature Datalogger - Extech Instruments.” [Online]. Available: <http://www.extech.com/display/?id=14721>. [Accessed: 02-Jun-2019].
- [43] “CompactDAQ Chassis - National Instruments.” [Online]. Available: <http://www.ni.com/en-tr/shop/select/compactdaq-chassis>. [Accessed: 02-Jun-2019].
- [44] T. Cebeci, “General Behavior of Turbulent Boundary Layers,” in *Analysis of Turbulent Flows with Computer Programs*, Elsevier, 2013, pp. 89–153.
- [45] S. . Patankar and D. . Spalding, “A calculation procedure for heat, mass and momentum transfer in three-dimensional parabolic flows,” *Int. J. Heat Mass Transf.*, vol. 15, no. 10, pp. 1787–1806, Oct. 1972.
- [46] R. Eppler, *Airfoil Design and Data*. Berlin, Heidelberg: Springer Berlin Heidelberg, 1990.
- [47] Inc. ANSYS, “ANSYS FLUENT Theory Guide,” *Release 18.2*, vol. 15317, no. November, pp. 373–464, 2013.

